CZECH TECHNICAL UNIVERSITY IN PRAGUE

Hydrodynamic simulations of X-ray generation and propagation in laser-produced plasmas

by

Martin Šach

Master's thesis

Faculty of Nuclear Sciences and Physical Engineering
Department of Physics

Supervisor: **doc. Ing. Milan Kuchařík, Ph.D.**
Consultants: **Ing. Jan Nikl, Ing. Miroslav Krůs, Ph.D.**
Field of study: **Physics and Technology of Thermonuclear Fusion**
July 2021

ČESKÉ VYSOKÉ UČENÍ TECHNICKÉ V PRAZE
FAKULTA JADERNÁ A FYZIKÁLNĚ INŽENÝRSKÁ
PRAHA 1 - STARÉ MĚSTO, BŘEHOVÁ 7 - PSČ 115 19

Katedra: fyziky *Akademický rok:* 2020/2021

ZADÁNÍ DIPLOMOVÉ PRÁCE

Student:	Bc. Martin Šach
Studijní program:	Aplikace přírodních věd
Obor:	Fyzika a technika termojaderné fúze
Název práce: (česky)	Hydrodynamické simulace generování a propagace rentgenového záření v laserovém plazmatu
Název práce: (anglicky)	Hydrodynamic simulations of X-ray generation and propagation in laser-produced plasmas

Pokyny pro vypracování:

V rámci výzkumného úkolu sestrojil student obecný N-hladinový model pro výpočet koeficientu zisku a ověřil jeho vlastnosti na jednoduchých hydrodynamických simulacích. Dále byl vyvinut model raytracingu, vhodný k modelování jak absorpce laseru, tak i šíření a zesilování rentgenového záření.

1) V rámci diplomové práce otestujte vyvinutou metodu raytracingu na vybraných jednoduchých úlohách a ověřte její robustnost a konvergenci.

2) Otestujte různé numerické metody pro výpočet gradientu hustoty a porovnejte jejich vliv na profil absorbované energie laseru.

3) Implementujte vyvinutou a otestovanou metodu do vybraného hydrodynamického kódu [1,2] a porovnejte ji s existujícími metodami absorpce.

4) Proveďte hydrodynamické simulace přípravy zesilujícího plazmatického prostředí s použitím N-hladinového modelu pro určení koeficientu zisku a výsledky porovnejte s literaturou [3].

5) Proveďte simulaci zesilování a propagace rentgenového záření v různých konfiguracích a zhodnoťte vlivy difrakce [4,5].

Doporučená literatura:

[1] R. Liska et al.: ALE Methods for Simulations of Laser-Produced Plasmas. FVCA VI, Springer Proceedings in Mathematics, Vol. 2, Nr. 4, pp. 57-73, Springer, 2011.

[2] J. Nikl et al.: Curvilinear high-order Lagrangian hydrodynamic code for the laser-target interaction, Europhysics Conference Abstracts, Vol. 42A, pp. P1, 2019.

[3] E. Oliva et al.: Hydrodynamic study of plasma amplifiers for soft-x-ray lasers: A transition in hydrodynamic behavior for plasma columns with widths ranging from 20 μm to 2 m. Phys. Rev. E, Vol. 82, pp. 056408, 2010.

[4] J.A. Plowes et al.: Beam modelling for x-ray lasers. Opt. Quantum Electron., Vol. 28, pp. 219-228, 1996.

[5] S. Le Pape et al.: Modeling of the influence of the driving laser wavelength on the beam quality of transiently pumped X-ray lasers, Opt. Commun., Vol. 219, pp. 323-333, 2003.

Jméno a pracoviště vedoucího diplomové práce:

doc. Ing. Milan Kuchařík, Ph.D., Katedra fyzikální elektroniky, FJFI ČVUT v Praze

Jména a pracoviště konzultantů:

Ing. Jan Nikl, Katedra fyzikální elektroniky, FJFI ČVUT v Praze

Ing. Miroslav Krůs, Ph.D., Ústav fyziky plazmatu, AV ČR

Datum zadání diplomové práce: 23.10.2020

Termín odevzdání diplomové práce: 03.05.2021

Doba platnosti zadání je dva roky od data zadání.

……
garant oboru

…….. ……..
vedoucí katedry *děkan*

V Praze dne 23.10.2020

Prohlášení

Prohlašuji, že jsem svou diplomovou práci vypracoval samostatně a použil jsem pouze podklady (literaturu, projekty, SW atd...) uvedené v přiloženém seznamu.

Nemám závažný důvod proti použití tohoto školního díla ve smyslu § 60 Zákona č. 121/2000 Sb., o právu autorském, o právech souvisejících s právem autorským a o změně některých zákonů (autorský zákon).

V Praze dne 27. 7. 2021 .....

podpis

Acknowledgements

I would like to thank my supervisor doc. Milan Kuchařík, as well as Jan Nikl, Ph.D. for their guidance and constant encouragement. I am grateful for the support, insightful feedback, and an incredible amount of time they spent with me consulting and pointing me in the right direction. Without them, I would be lost in the world of computer simulations. Also, thank you to Miroslav Krůs, Ph.D. for introducing me to the world of x-ray lasers and providing the much-appreciated resources to study the topic.

Název práce:

Hydrodynamické simulace generování a propagace rentgenového záření v laserovém plazmatu

Autor: Martin Šach

Obor: Fyzika a technika termojaderné fúze

Druh práce: Diplomová práce

Vedoucí práce: doc. Ing. Milan Kuchařík, Ph.D., Katedra fyzikální elektroniky, FJFI ČVUT v Praze

Konzultanti: Ing. Jan Nikl, Katedra fyzikální elektroniky, FJFI ČVUT v Praze, Ing. Miroslav Krůs, Ph.D., Ústav fyziky plazmatu, AV ČR

Abstrakt: Hydrodynamické simulace v kombinaci s metodou trasování paprsků představují užitečný nástroj pro studium plazmatu jako média vhodného k zesilování rentgenového záření. Modelováním plazmatu vzniklého interakcí laserového impulzu s pevným terčem a následnou simulací průchodu a zesílení rentgenového pulzu tímto médiem mohou být získány užitečné poznatky o celém procesu. V této práci je zahrnuta formulace hydrodynamického popisu pomocí metody konečných prvků a je představeno rozšíření o modely zesilování a absorpce záření pomocí metody trasování paprsků. Důraz je kladen na metody výpočtu gradientu elektronové hustoty a zhodnocení jejich vlivu na modelování absorpce laserového záření. Dále je prezentováno několik úloh testujících implementaci daných modelů. Konečně jsou v práci předvedeny výsledky simulací zesilování rentgenového pulzu na konkrétním zářivém přechodu v neonu-podobných iontech v plazmatu vytvořeném interakcí tří laserových pulsů s pevným železným terčem. Speciální pozornost je věnována difrakci rentgenového pulzu při průchodu zesilujícím médiem.

Klíčová slova: Lagrangeovská hydrodynamika, trasování paprsků, plazmové simulace, metoda konečných prvků, rentgenový laser

Title:

Hydrodynamic simulations of X-ray generation and propagation in laser-produced plasmas

Author: Martin Šach

Abstract: Hydrodynamic plasma simulations in combination with ray-tracing methods are a useful tool to study plasma as a medium suitable for x-ray pulse radiation amplification. Modeling of plasma produced by a laser beam interacting with a solid target and the subsequent simulation of amplification of an x-ray pulse traveling through this medium can provide useful insights into the whole process. In this thesis, a formulation of hydrodynamic description, using the finite element method, is summarized and additional models of amplification and absorption of radiation using a ray-tracing method are presented. An emphasis is put on the various electron density gradient calculation methods, influencing the radiation absorption modeling. Next, several problems are devised to test the implemented models. Finally, results of an x-ray pulse amplification on a particular lasing transition of neon-like ions in the plasma generated by three laser pulses interacting with a solid iron target are presented. Special attention is paid to diffraction of the x-ray pulse traversing the amplifying media.

Key words: Lagrangian hydrodynamics, ray-tracing, plasma simulations, finite elements method, x-ray laser

Contents

1 Introduction **1**

2 Lagrangian hydrodynamic model **5**
2.1 Euler equations in Lagrangian coordinates . . . 5
2.2 Semi-discrete formulation of the euler equations . . . 7
2.3 Heat transfer model . . . 9
2.4 Collisional frequency model . . . 10
2.5 Artificial viscosity . . . 11
2.6 Time stepping scheme and dynamic time step . . . 12

3 Ray-tracing approach to laser simulations **15**
3.1 Geometric optics approximation . . . 15
3.2 Refractive index model . . . 16
3.3 Ray-tracing algorithm . . . 16
3.4 Integral solution of the ray equation . . . 18
3.5 Special case analytic solutions of the eikonal equation . . . 21
3.5.1 Analytic ray trajectory in a constant electron density gradient . . . 22
3.5.2 Analytic ray trajectory in a quadratic electron density . . . 22

4 Absorption models to simulate laser-plasma interaction **25**
4.1 Associating power to the rays . . . 25
4.2 Model of absorption via inverse bremsstrahlung . . . 26
4.3 Resonant absorption model . . . 27
4.4 Model of absorption based on Fresnel equations . . . 28

5 X-ray gain coefficient model **31**
5.1 Description of the model . . . 31
5.1.1 Spectral line broadening . . . 32
5.1.2 Population inversion and weighted oscillator strength . . . 33
5.2 Verification of the model . . . 34
5.3 Predictions of the model . . . 34

6 Gradient calculation methods **37**
6.1 Method using the Green's theorem . . . 37
6.2 Method based on the finite element formulation . . . 39
6.3 Method based on the least-squares formulation . . . 40
6.4 Study of the convergence of the methods . . . 41
6.4.1 Convergence of the method using the Green's theorem . . . 43

6.4.2 Convergence of the method using the finite element formulation . . 44
6.4.3 Convergence of the method using the least-squares formulation . . 44
6.5 Method imprinting into trajectory estimation 46

7 Comparison with existing methods **51**
7.1 Comparison with the WKB approximation 51
7.2 Comparison with a finite difference simulation 52

8 Simulation of realistic plasma with positive x-ray gain coefficient **55**
8.1 Parameters of the simulation 56
8.2 Results of the simulation 57

9 Evaluation of the diffraction effects in x-ray propagation **61**
9.1 Difficulties using the linear ray-tracing algorithm to estimate diffraction . 61
9.2 Semi-analytic approach to the estimation of the diffraction effects 63

10 Conclusion **67**

Bibliography **71**

Physical Constants

c	speed of light	$\mathrm{cm} \cdot \mathrm{s}^{-1}$
k_b	Boltzmann constant	$\mathrm{erg} \cdot \mathrm{eV}^{-1}$
e	electron charge	statC
m_e	electron mass	g
m_u	atomic mass unit	g
$\hbar$	reduced Planck constant	$\mathrm{erg} \cdot \mathrm{Hz}^{-1}$

Chapter 1

Introduction

A source of coherent, polarized radiation in the near x-ray or extreme ultraviolet region of the electromagnetic spectrum is collectively referred to as an x-ray laser. Mastering the technology of an sufficiently intense x-ray lasers, may bring ground-breaking advances across a wide range of scientific fields. For example, a great demand for such technology is in the microchip industry, where lasers with short wavelength could be used to manufacture integrated circuits with sub-optical precision and enable more transistors to be fitted into a given volume through a process called microlithography [1]. Further, possible applications are in biology and material sciences, where an x-ray laser with good optical properties can be used to capture images with a previously impossible level of detail. This can be used for normal imagining as well as for holographic reconstruction of 3D structures [2]. In material sciences, besides offering a better resolution, the laser can be used to probe materials opaque for conventional methods. Last but certainly not least, a femtosecond x-ray pulse can be used to snapshot an image of electron orbitals during a chemical reaction, bringing new advances in the field of chemistry and physics alike.

Numerous approaches exist to generation of coherent near x-ray and extreme ultraviolet radiation. The most notable one is known as the Free Electron Laser (FEL). Invented by John Madey, it was first demonstrated in the 1970s at the Stanford University. It relies on the fact that an initial random field of spontaneous radiation can be amplified by an electron beam traveling through an undulator (a device generating a periodic magnetic field) [3]. Another possibility is to use the high harmonic generation (HHG) approach where higher harmonic frequencies are generated when a conventional laser passes through an ionized gas. Most other methods of generating near x-ray or extreme ultraviolet radiation with good optical and spectral properties facilitate certain special gain media to amplify the pulse. Among these, is the approach described in this

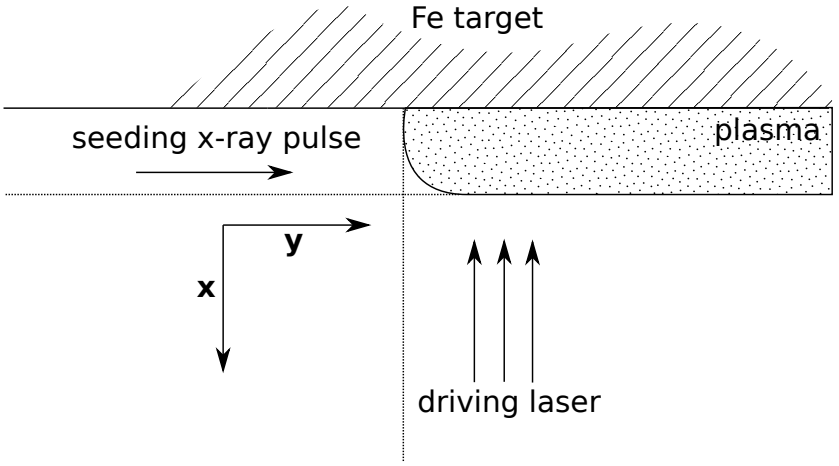

FIGURE 1.1: The geometry of plasma generated by the driving laser as an amplification medium for the seeding X-ray pulse as already shown in [6]

work, where a plasma generated by a laser interacting with a solid target is used in place of the gain medium. This approach is very promising especially when generation of very short, intense pulses is considered [4].

To fully utilize the potential of the plasma gain medium, usually, a seeding pulse is used to initiate the amplification. Following this approach, advantageous optical properties of the seeding pulse (polarization, coherence, etc.) are directly translated to the amplified pulse. The seeding can be prepared by one of the previously mentioned methods. The most frequent approach is to use HHG generation, as the driving pulse producing the plasma can then also serve as a seed [5], after passing through an ionized gas.

In this work, we are concerned about developing a suitable tool for the optimization of the plasma gain medium properties. The goal is to achieve the maximal possible amplification of the seeding pulse. The spatial configuration previously described in [6] is shown in Figure 1.1. Intense laser (driver), perpendicular to a planar solid target, produces a plasma, which under the right conditions can serve as the gain medium. Then a seeding pulse is propagated in the direction parallel to the target surface.

This work is a continuation of the previous efforts [7], [6]. We model the plasma using a hydrodynamic code formulated in the framework of the finite element method (FEM). In principle, the formulation of the code can be used for simulations in an arbitrary number of dimensions (3, 2, 1), but for practical reasons we limit ourselves to 2D in this work. To account for the interaction with both the driving laser and the seeding pulse a ray-tracing algorithm is implemented. This algorithm heavily relies on the particular approximation of electron density gradient. Thus, methods of gradient calculation

are studied in more detail. Additionally, several models of energy exchange are used, including a model of x-ray gain coefficient, to simulate the seeding pulse amplification.

In chapter 2, a finite element formulation of the Euler equations is presented and the discretization scheme is summarized. Additionally, several physical models used alongside the Euler equations are described, particularly the heat transfer model and the collisional frequency model. Next, the artificial viscosity and time the stepping scheme are discussed and the dynamic time step control is reviewed.

The ray-tracing simulations of a laser interacting with a plasma are addressed in chapter 3. The previously used approach [7] is reviewed and extended by adding a more fundamental equation, the eikonal equation. The derivation [8] of an analytic solution to the eikonal equation, in a special index of refraction profile, is shown.

We extend the ray-tracing algorithm with several models of absorption in chapter 4. There, the previously used models of bremsstrahlung and resonance absorption are described and the new model of Fresnel absorption is introduced.

The modeling of the seeding pulse amplification is the main topic of chapter 5, where a formula for the gain coefficient based on the M level model of energy levels populations is reviewed.

In chapter 6, the details of several gradient calculation methods are formulated. Then, the convergence of the methods is evaluated. Finally, it is studied how the gradient calculation methods influence the ray-tracing algorithm and thus the modeling of laser absorption.

The rest of the work is devoted to the numerical results. In chapter 7, the robustness of the absorption method is tested on the simulation previously described in [9]. Next, several simulations of more realistic plasma conditions are summarized in chapter 8 and the results are compared with [10]. Lastly, the results of simulations, where diffraction effects in the x-ray propagation can be observed, are shown and discussed in chapter 9.

Chapter 2

Lagrangian hydrodynamic model

In this chapter, the Euler equations are introduced and models used in the simulations are summarized. The whole description is given in Lagrangian coordinates. In the Lagrangian description, the coordinates evolve with the simulated plasma, and the simulated domain changes in time. Proper introduction of the coordinates has been previously given in [7]. To describe a phenomenon in Lagrangian coordinates the use of material derivative [11] is typical

$$\frac{\mathrm{d}\alpha}{\mathrm{d}t} = \frac{\partial\alpha}{\partial t} + \mathbf{v}\cdot\boldsymbol{\nabla}\alpha, \tag{2.1}$$

where α is a quatity associated with the fluid and $\mathbf{v}$ is the particle velocity in the Eulerian reference frame.

2.1 Euler equations in Lagrangian coordinates

First, let us briefly address mass conservation. It can be proved [11] that in the Lagrangian coordinates, given a starting volume U and the deformation of this volume with fluid motion $U(t)$, mass in this volume never changes. Formally, it can be derived that this may be expressed in differential form as

$$\frac{1}{\rho}\frac{\mathrm{d}\rho}{\mathrm{d}t} = -\boldsymbol{\nabla}\cdot\mathbf{v} \tag{2.2}$$

where ρ is the mass density of the fluid. This particular property of Lagrangian coordinates can be used to establish time dependent density $\rho(\tilde{x},t)$ as [11]

$$\rho(\tilde{x},t) = \rho_0(\tilde{x})/\left|\tilde{J}(\tilde{x},t)\right|, \tag{2.3}$$

where $\tilde{x}$ is the Lagrangian coordinate, $\rho_0(\tilde{x})$ is the initial density of the fluid and $\left|\tilde{J}(\tilde{x},t)\right|$ is the Jacobian of the coordinate transformation

$$\left|\tilde{J}(\tilde{x},t)\right| = |\boldsymbol{\nabla}_{\tilde{x}} x|. \tag{2.4}$$

A two temperature model, following [12] is used, instead of the original one temperature model in [11], meaning electrons and ions have different temperatures. This leads to the following differential form expression of conservation of momentum

$$\rho \frac{\mathrm{d}\mathbf{v}}{\mathrm{d}t} = \boldsymbol{\nabla}(\sigma^{(\mathrm{e})} + \sigma^{(\mathrm{i})}) \tag{2.5}$$

where $\sigma^{(\mathrm{e,i})}$ is a stress tensor dependent on the plasma pressure and viscosity and is treated separately for electrons and ions.

Another change to the original algorithm [11] is in the equation for conservation of energy. It is advantageous to set electron and ion temperatures T_e and T_i as the main variables. This avoids a computationally intensive inversion of the equation of state in simulations following this description. Also, in the two-temperature model an energy exchange term needs to be added to the equations. Altogether, the equations originating from the conservation of energy read [12]

$$\rho c_{\mathrm{Ve}} \frac{\partial T_\mathrm{e}}{\partial t} = \sigma^{(\mathrm{e})} : \boldsymbol{\nabla}\mathbf{v} + G_{\mathrm{ei}}(T_\mathrm{i} - T_\mathrm{e}) - \boldsymbol{\nabla} \cdot (\mathbf{q}_\mathrm{e} + \mathbf{S}), \tag{2.6}$$

$$\rho c_{\mathrm{Vi}} \frac{\partial T_\mathrm{i}}{\partial t} = \sigma^{(\mathrm{i})} : \boldsymbol{\nabla}\mathbf{v} + G_{\mathrm{ie}}(T_\mathrm{e} - T_\mathrm{i}), \tag{2.7}$$

where c_{Ve}, c_{Vi} are the electron and iont specific heats, G_{ei} and G_{ie} are the energy exchange terms, $\mathbf{q_e}$ is the electron heat flux given by a model of heat transfer and $\mathbf{S}$ is the Poynting vector given by a model of laser absorption. Note that $\boldsymbol{\nabla}\mathbf{v}$ is a second order tensor and ":" denotes a double dot product.

Additionally, an equation giving a description of the stress tensor in terms of state variables needs to be provided. In the simplest case, this can be facilitated by the equation of state (EOS)

$$\sigma^{(\mathrm{e,i})} = -p^{(\mathrm{e,i})}\mathbb{I}, \quad p_\mathrm{e} = EOS(\rho, T_e), \quad p_\mathrm{i} = EOS(\rho, T_i). \tag{2.8}$$

A slightly more complicated formula is used if a model of artificial viscosity is considered, presented further in section 2.5.

To complete the system of equations and to be able to calculate the Jacobian of the transformation to the Lagrangian frame of reference, the equation of motion is used

$$\frac{\mathrm{d}\mathbf{x}}{\mathrm{d}t} = \mathbf{v}. \tag{2.9}$$

2.2 Semi-discrete formulation of the euler equations

For the plasma simulations, a hydrodynamic code PETE2 [12] is chosen. It is a hydrodynamic code developed in the framework of the finite element method (FEM) and uses discretization described in [11].

Following [11], two discrete finite element spaces are used to obtain a semidiscrete (discretized only in spatial coordinates) formulation in the framework of the finite element method

$$\mathcal{V}(t) \subset \left[H^1(\Omega(t)\right]^d, \text{ with basis } \left\{\boldsymbol{\psi}^{(k)}\right\}_{k=1}^{N_\mathcal{V}}, \tag{2.10}$$

$$\mathcal{E}(t) \subset L_2(\Omega(t)), \text{ with basis } \left\{\varphi^{(j)}\right\}_{j=1}^{N_\mathcal{E}}, \tag{2.11}$$

where d is the dimension of the problem and $\Omega(t)$ is the moving Lagrangian domain. Space $\mathcal{V}$ is often referred to as the kinematic and space $\mathcal{E}$ is usually called the thermodynamic space. Using $\sigma = \sigma^{(\mathrm{e})} + \sigma^{(\mathrm{i})}$ for brevity and using a Galerkin approach [11], the equation (2.5) is multiplied by a basis test function $\boldsymbol{\psi}^{(k)}$, integrated over the moving domain and Green's theorem is applied

$$\int_{\Omega(t)} \rho \frac{\mathrm{d}v_i}{\mathrm{d}t} \psi_i^{(k)} \mathrm{d}V = -\int_{\Omega(t)} \sigma_{i,j} : \frac{\partial \psi_j^{(k)}}{\partial x_i} \mathrm{d}V + \int_{\partial\Omega(t)} n_i \sigma_{ij} \psi_j^{(k)} \mathrm{d}S \quad \forall k \tag{2.12}$$

where $\mathbf{n}$ is a normal vector to $\partial\Omega(t)$. Assuming the boundary term vanishes and expanding the velocity in the moving basis

$$v_i = \sum_m v^{(m)} \psi_i^{(m)}, \quad \text{where } v^{(m)} \in \mathbb{R} \tag{2.13}$$

a semidiscrete formulation of the momentum conservation equation is obtained

$$\sum_m \frac{\mathrm{d}v^{(m)}}{\mathrm{d}t} \int_{\Omega(t)} \rho \psi_i^{(m)} \psi_i^{(k)} \mathrm{d}V = -\int_{\Omega(t)} \sigma_{i,j} \frac{\partial \psi_j^{(k)}}{\partial x_i} \mathrm{d}V \quad \forall k \tag{2.14}$$

Using the notion of a mass matrix this can be rewritten as

$$\mathbb{M}_\mathcal{V} \frac{\mathrm{d}v^{(1\ldots N_\mathcal{V})}}{\mathrm{d}t} = -\int_{\Omega(t)} \sigma : \boldsymbol{\nabla} \boldsymbol{\psi}^{(1\ldots N_\mathcal{V})} \mathrm{d}V, \tag{2.15}$$

where mass matrix $\mathbb{M}_{\mathcal{V}}$ is defined as

$$(\mathbb{M}_{\mathcal{V}})_{mk} = \int_{\Omega(t)} \rho \boldsymbol{\psi}^{(m)} \boldsymbol{\psi}^{(k)} \mathrm{d}V. \tag{2.16}$$

Note that $v^{(1\ldots N_{\mathcal{V}})}$ is a column vector formed by coefficients $v^{(m)}$.

Virtually the same procedure can be performed to obtain a semidiscrete formulation of the energy conservation equations. The expansion of temperature in the thermodynamic basis has the following form

$$T_{\mathrm{e}} = \sum_m T_{\mathrm{e}}^{(m)} \varphi^{(m)} \tag{2.17}$$

$$T_{\mathrm{i}} = \sum_m T_{\mathrm{i}}^{(m)} \varphi^{(m)} \tag{2.18}$$

and the semidiscrete formulation is

$$\begin{aligned} \sum_m \frac{\mathrm{d}T_{\mathrm{e}}^{(m)}}{\mathrm{d}t} \int_{\Omega(t)} c_{\mathrm{Ve}} \rho \varphi^{(m)} \varphi^{(j)} \mathrm{d}V = \sum_m v^{(m)} \int_{\Omega(t)} \sigma_{i,j}^{(\mathrm{e})} \frac{\partial \psi_j^{(m)}}{\partial x_i} \varphi^{(j)} \mathrm{d}V + \\ + \sum_m (T_{\mathrm{i}}^{(m)} - T_{\mathrm{e}}^{(m)}) \int_{\Omega(t)} G_{\mathrm{ei}} \varphi^{(m)} \varphi^{(j)} \mathrm{d}V + \int_{\Omega(t)} (\mathbf{q}_{\mathrm{e}} + \mathbf{S}) \boldsymbol{\nabla} \varphi^{(j)} \mathrm{d}V \quad \forall j \end{aligned} \tag{2.19}$$

for electrons and

$$\begin{aligned} \sum_m \frac{\mathrm{d}T_{\mathrm{i}}^{(m)}}{\mathrm{d}t} \int_{\Omega(t)} c_{\mathrm{Vi}} \rho \varphi^{(m)} \varphi^{(j)} \mathrm{d}V = \sum_m v^{(m)} \int_{\Omega(t)} \sigma_{k,l}^{(\mathrm{i})} \frac{\partial \psi_l^{(m)}}{\partial x_k} \varphi^{(j)} \mathrm{d}V + \\ + \sum_m (T_{\mathrm{e}}^{(m)} - T_{\mathrm{i}}^{(m)}) \int_{\Omega(t)} G_{\mathrm{ie}} \varphi^{(m)} \varphi^{(j)} \mathrm{d}V \quad \forall j \end{aligned} \tag{2.20}$$

for ions. By defining the following matrices and vector

$$\left(\mathbb{M}_{\mathcal{E}}^{(\mathrm{e,i})}\right)_{mj} = \int_{\Omega(t)} c_{\mathrm{Vei}} \rho \varphi^{(m)} \varphi^{(j)} \mathrm{d}V, \tag{2.21}$$

$$\left(\mathbb{F}_{\mathcal{E}}^{(\mathrm{e,i})}\right)_{mj} = \int_{\Omega(t)} \sigma_{k,l}^{(\mathrm{e,i})} \frac{\partial \psi_l^{(m)}}{\partial x_k} \varphi^{(j)} \mathrm{d}V \tag{2.22}$$

$$\mathbb{G}_{mj}^{\mathrm{ie}} = \int_{\Omega(t)} G_{\mathrm{ie}} \varphi^{(m)} \varphi^{(j)} \mathrm{d}V \tag{2.23}$$

$$s^{(j)} = \int_{\Omega(t)} (\mathbf{q}_{\mathrm{e}} + \mathbf{S}) \boldsymbol{\nabla} \varphi^{(j)} \mathrm{d}V \tag{2.24}$$

the set of equations including the momentum conservation can be rewritten in a compact algebraic form

$$\mathbb{M}_{\mathcal{V}} \frac{\mathrm{d}v^{(1\dots N_{\mathcal{V}})}}{\mathrm{d}t} = -\mathbb{F} \cdot 1^{(1\dots N_{\mathcal{V}})} \tag{2.25}$$

$$\mathbb{M}_{\mathcal{E}}^{(\mathrm{e})} \frac{\mathrm{d}T_{\mathrm{e}}^{(1\dots N_{\mathcal{E}})}}{\mathrm{d}t} = \left(\mathbb{F}^{(\mathrm{e})}\right)^T \cdot v^{(1\dots N_{\mathcal{V}})} + \mathbb{G}^{\mathrm{ie}}\left(T_{\mathrm{e}}^{(1\dots N_{\mathcal{E}})} - T_{\mathrm{i}}^{(1\dots N_{\mathcal{E}})}\right) + s^{(1\dots N_{\mathcal{E}})} \tag{2.26}$$

$$\mathbb{M}_{\mathcal{E}}^{(\mathrm{i})} \frac{\mathrm{d}T_{\mathrm{i}}^{(1\dots N_{\mathcal{E}})}}{\mathrm{d}t} = \left(\mathbb{F}^{(\mathrm{i})}\right)^T \cdot v^{(1\dots N_{\mathcal{V}})} + \mathbb{G}^{\mathrm{ei}}\left(T_{\mathrm{i}}^{(1\dots N_{\mathcal{E}})} - T_{\mathrm{e}}^{(1\dots N_{\mathcal{E}})}\right) \tag{2.27}$$

$$\frac{\mathrm{d}x}{\mathrm{d}t} = v \tag{2.28}$$

To assemble the matrices and solve the resulting system, a finite element library MFEM [13] is used.

It remains to address the terms $\mathbf{S}$ and $\mathbf{q}_{\mathrm{e}}$, specify the stress tensor (including artificial viscosity), and discretize the equations in time.

2.3 Heat transfer model

Instead of evaluating $\mathbf{q}_{\mathrm{e}}$ directly and adding it to the equations, an operator splitting technique similar to the one used in [7] is employed. It enables solving the heat equation separately

$$\rho c_{\mathrm{Ve}} \frac{\mathrm{d}T_{\mathrm{e}}}{\mathrm{d}t} + \boldsymbol{\nabla} \cdot \mathbf{q}_e = 0. \tag{2.29}$$

Furthermore, Fourier's law of heat conduction [14] is used to determine the heat flux $\mathbf{q}_{\mathrm{e}}$

$$\mathbf{q}_{\mathrm{e}} + \kappa(T)\boldsymbol{\nabla} T = 0, \tag{2.30}$$

where $\kappa(T)$ is a heat conductivity coefficient. As the coefficient is a function of temperature $\kappa \sim T^{\alpha}$ the equation is nonlinear. To linearize the problem, the following transformation [14] is used

$$\bar{T}_{\mathrm{e}} = T_{\mathrm{e}}^{\alpha+1}, \quad \bar{\kappa} = \frac{\kappa}{\alpha+1} T_{\mathrm{e}}^{-\alpha}, \quad \bar{c}_{\mathrm{Ve}} = \frac{c_{\mathrm{Ve}}}{\alpha+1} T^{-\alpha} \tag{2.31}$$

and the equations keep their original form, only using the transformed variables in place of the original values.

A formulation of these equations in the framework of the finite element method is used in the code PETE2 to actually solve the heat transfer equation. This is not a trivial task and is not described in this work. Details are in [14].

It is possible for the scheme to generate non-physically large heat fluxes. A limit is thus imposed for the flux to not exceed the free streaming value [14]

$$|\mathbf{q}_{\max}| = f_{\lim} n_e k_b T_e v_{\text{th}}, \tag{2.32}$$

where $f_{\lim}$ is an empirical constant set to 0.1 throughout this work and v_{th} is the thermodynamical velocity coresponding to temperature T_e. If the limit is exceeded, the value of κ is rescaled according to [14]

$$\kappa = \kappa \min\left(1, \frac{|\mathbf{q}_{\max}|}{|\mathbf{q}_e|}\right) \tag{2.33}$$

and the calculation is repeated.

2.4 Collisional frequency model

An electron-ion collisional frequency model is needed for both the energy exchange terms in the Euler equations and the refractive index model shown in chapter 3. The classic Spitzer-Harm frequency model is used as an approximation of collision frequency of high temperature plasma [15].

$$\nu_{\text{SH}} = \frac{4}{3}\sqrt{2\pi}\frac{Ze^4 m_e n_e}{(m_e k_b T_e)^{3/2}} \ln(\Lambda), \tag{2.34}$$

where the electron density n_e is obtained form the mass density ρ and mean ionization state Z

$$n_e = \frac{Z\rho}{A m_u}. \tag{2.35}$$

Here A is the nucleon number of the given material.

This model is not valid for low temperature plasma as it diverges at $T = 0$. Especially at the beginning of a simulation, this is the case and it must be addressed. An improved model based on the Eidmann approximation is used to resolve the issue. The Eidmann collision frequency between electrons and phonons is defined as[16]

$$\nu_{\text{ef}} = 2k_s \frac{e^2 k_b T_i}{\hbar^2 v_F} \tag{2.36}$$

$$v_F = \frac{\hbar \sqrt[3]{3\pi^2 n_e}}{m_e}. \tag{2.37}$$

Finally, the resulting collisional frequency is taken to be the harmonic mean of the previously introduced models

$$\nu_{\mathrm{ei}} = \frac{\nu_{\mathrm{SH}}\nu_{\mathrm{ef}}}{\nu_{\mathrm{SH}} + \nu_{\mathrm{ef}}}. \tag{2.38}$$

2.5 Artificial viscosity

Artificial viscosity is a diffusion term introduced into the Euler equations to enable the simulation of shock wave propagation, as the numerical solution would oscillate heavily otherwise. In the same way, as in the original algorithm, [11] the artificial viscosity is implemented by introducing an artificial stress tensor σ_a to the total stress tensor σ (for both electrons and ions, the superscript is omitted for brevity)

$$\sigma(\mathbf{x}) = -p(\mathbf{x})\mathbb{I} + \sigma_a(\mathbf{x}). \tag{2.39}$$

To establish the artificial stress, a symmetrized velocity gradient tensor is defined

$$\epsilon(\mathbf{v}) = \frac{1}{2}(\boldsymbol{\nabla}\mathbf{v} + \mathbf{v}\boldsymbol{\nabla}). \tag{2.40}$$

The tensor has the following spectral decomposition

$$\epsilon(\mathbf{v}) = \sum_k \lambda_k \mathbf{s}_k \otimes \mathbf{s}_k, \quad \mathbf{s_i} \cdot \mathbf{s_j} = \delta_{ij}, \tag{2.41}$$

where λ_k are the eigenvalues and $\mathbf{s}_k$ are the eigenvectors of the tensor. The artificial viscosity model used throughout this work is what is referred to as type 4 model in the original work [11]. It is defined in the following way

$$\sigma_a = \sum_k \mu_{s_k} \lambda_k \mathbf{s}_k \otimes \mathbf{s}_k, \tag{2.42}$$

where a directional viscosity coefficient μ_{s_k} plays a key role. A general form of the coefficient is

$$\mu_s \equiv \rho\Big\{ q_2 l_s^2 |\Delta_s \mathbf{v}| + q_1 \psi_0 \psi_1 l_s c_s \Big\}, \tag{2.43}$$

where q_1, q_2 are linear and quadratic scaling coefficients, here, both are set to 1, c_s is the speed of sound evaluated at $\mathbf{x}$ and l_s is known as directional length scale and is evaluated as [11]

$$l_s = l_0 \frac{|\mathbf{s}|}{\left|\tilde{J}^{-1}\mathbf{s}\right|}. \tag{2.44}$$

The quantity l_0 is the initial scale and can be defined in various ways depending on the used mesh. For example, for a close to uniform mesh, this can be defined as a global

constant. The Jacobi matrix is evaluated similar to (2.4) and inverted. In practice, the inversion is performed on a zone-by-zone basis. Finally, $|\mathbf{s}|$ is the directional measure of compression. It can be shown that for $\mathbf{s_k}$ this is given by λ_k [11].

It remains to explain the meaning of terms ψ_0 and ψ_1. The term ψ_1 is called a compression switch and causes the artificial viscosity to vanish at points in expansion [11]

$$\psi_1 = \begin{cases} 1, & \text{if } \Delta_s \mathbf{v} < 0 \\ 0, & \text{otherwise.} \end{cases} \tag{2.45}$$

The term ψ_0 is called a vorticity measure and causes the artificial viscosity to vanish for purely vortical flows [11]

$$\psi_0 = \frac{|\boldsymbol{\nabla} \cdot \mathbf{v}|}{||\boldsymbol{\nabla} \mathbf{v}||}. \tag{2.46}$$

2.6 Time stepping scheme and dynamic time step

Similarly to [11] a vector of the main variables is introduced

$$\mathbf{Y} = \begin{pmatrix} \mathbf{v} \\ T_\mathrm{e} \\ T_\mathrm{i} \\ \mathbf{x} \end{pmatrix} \tag{2.47}$$

The Euler equations in a semidiscrete form (2.25) - (2.28) can be symbolically denoted as

$$\frac{d\mathbf{Y}}{dt} = \mathcal{F}(\mathbf{Y}, t), \tag{2.48}$$

where $\mathcal{F}$ is the right-hand side of the equations obtained by inverting the mass matrices on the left-hand side and moving them to the right-hand side. As noted in [11], standard discretization schemes such as explicit Runge-Kutta methods can be applied to discretize the equations in the time domain and obtain a fully discretized scheme.

Although the used hydrodynamic code PETE2 [12] supports multiple discretization schemes, the scheme of choice for this work is a modified midpoint Runge-Kutta second-order scheme (RK2-average). The original RK2 scheme has the following form [11]

$$\mathbf{Y}^{n+\frac{1}{2}} = \mathbf{Y} + \frac{\Delta t}{2} \mathcal{F}(\mathbf{Y}^n, t^n) \tag{2.49}$$

$$\mathbf{Y}^{n+1} = \mathbf{Y} + \frac{\Delta t}{2} \mathcal{F}(\mathbf{Y}^{n+\frac{1}{2}}, t^{n+\frac{1}{2}}), \tag{2.50}$$

where Δt is the dicrete time step. The modification is in the second part of the stepping scheme where first a new velocity $\mathbf{v}^{n+1}$ is calculated using the original scheme. Then, instead of using the first half step velocity $\mathbf{v}^{n+\frac{1}{2}}$ to evaluate the rest of the equations, an averaged velocity is used

$$\bar{\mathbf{v}}^{n+\frac{1}{2}} = \frac{\mathbf{v}^{n+1} + \mathbf{v}^{n}}{2}. \tag{2.51}$$

It turns out that this particular scheme is significantly more stable than the original scheme. For more details see [11].

Finally, the time step evaluation needs to be addressed as it is not constant throughout the simulation. To facilitate the automatic time step control, several criteria for time step repetition are employed.

The first and most basic criterion is the evaluation of time step estimate

$$\tau^n = \min_{\mathbf{x}} \alpha \left(\frac{c_\mathrm{s}(\mathbf{x})}{h_\mathrm{min}} + \alpha_\mu \frac{\mu_s(\mathbf{x})}{\rho(\mathbf{x}) h_\mathrm{min}^2(\mathbf{x})} \right)^{-1}, \tag{2.52}$$

where $h_\mathrm{min}(x)$ is the minimal singular value of $J_z(\tilde{\mathbf{x}})$ (Jacobian of the transformation in the discrete zone z), c_s is the speed of sound, ρ is density and α, α_μ are CFL constants in this work set to 0.5 and 2.5 respectively. The repetition condition has the following form: given a state $\mathbf{Y}^n$ evaluate the state $\mathbf{Y}^{n+1}$ using Δt and corresponding time step estimate τ, if $\Delta t \geq \tau^n$ trigger the time step repetition.

The second criterion is on the specific internal energy change. Even though specific internal energy e as defined here [11] is not considered a main variable in this work, it is still evaluated during the simulation. It is then used to specify the following

$$\varepsilon^n = \max_{\mathbf{x}} \frac{e^n(\mathbf{x}) - e^{n-1}(\mathbf{x})}{e^n(\mathbf{x})}. \tag{2.53}$$

The repetition is triggered when the value of ε^n exceeds a certain threshold δ. Usually the value $\delta = 0.7$ is used. This ensures that the energy increase in a single zone due to laser absorption is not exceedingly high during the simulation. It also makes sure that the laser is absorbed in an appropriate amount of time steps sampling its intensity time profile well enough.

The last criterion is purely practical. When during the simulation an invalid state occurs, such that the solution of the system of equations diverges, repetition of the step is triggered, in hope it resolves the issue.

If one of the conditions is met, the time step is set to $\Delta t = \beta_1 \Delta_t$ and the whole procedure of time stepping and estimating τ^n is repeated. On the other hand, if none of the conditions is met, and $\Delta t \leq \gamma \tau^n$, the time step is increased according to $\Delta t = \beta_2 \Delta t$.

In any other case the simulation continues with an unmodified time step. The constants are set following [11] to $\beta_1 = 0.85$, $\beta_2 = 1.02$ and $\gamma = 0.8$.

Chapter 3

Ray-tracing approach to laser simulations

In this chapter, the ray-tracing approach to modeling the laser propagation in the plasma is described. The aim is to enable both, the driving, and the x-ray pulse simulations. The models and conclusions from previous work [6] are covered and important details, concerning the inclusion of the models to the hydrodynamic model, are added. Also, analytic solutions of the ray trajectories are found, which serves for a later reference.

3.1 Geometric optics approximation

The aim here is to include a model of radiation propagation in a hydrodynamic simulation. Different approaches are possible in general, but the ray-tracing approach is chosen in this work for its generality and ability to model a wide range of plasma processes. This approach relies on the fact, that the plasma characteristic scales are large compared to the wavelength of the radiation λ. In this approach, it is assumed that a geometric optics approximation can be used [6], where the wave nature of the radiation is neglected and it is expected that the radiation propagates in the form of rays. In this approximation, laser radiation is described as a set of independent rays, each carrying its share of power of the original laser beam.

A single ray is then fully described by the solution of the ray equation [17]

$$\frac{\mathrm{d}}{\mathrm{d}s}\left(n\frac{\mathrm{d}\mathbf{r}}{\mathrm{d}s}\right) = \boldsymbol{\nabla} n, \tag{3.1}$$

where $\mathbf{r}$ describes the trajectory of the ray, n is the refraction index of the plasma and s is a parameter defined along the trajectory of the ray.

Another, more fundamental description of radiation propagation is the eikonal equation [8]

$$|\boldsymbol{\nabla} S|^2 = n^2, \tag{3.2}$$

where S is the so-called eikonal. Eikonal S is a scalar function of $\mathbf{r}$ and its definition originates from the following description of a harmonic wave [18]

$$\mathbf{E} = \mathbf{E}_0 \exp\big(ik_0 S(\mathbf{r}/c)\big) \exp(-i\omega t), \tag{3.3}$$

where $\mathbf{E}$ is the electric field, $\mathbf{E}_0$ is slowly varying amplitude, k is the wave number, ω is the angular frequency and t is time.

It can be shown that the equation (3.1) can be derived using the equation (3.3). Both equations are used in this work to devise special case solutions for the ray trajectory.

3.2 Refractive index model

The mode of refractive index of the plasma is a key part of simulations using ray-tracing to calculate the effects of radiation propagation. It represents a connection between the state variables of the plasma and the index of refraction. In this and the previous works [6], the model of cold plasma taken from [9] is used. It states that the permittivity of the plasma is

$$\varepsilon = 1 - \frac{\omega_\mathrm{p}^2}{\omega^2 + \nu_\mathrm{ei}^2} + i\frac{\nu_\mathrm{ei}}{\omega}\frac{\omega_\mathrm{p}^2}{\omega^2 + \nu_\mathrm{ei}^2}, \tag{3.4}$$

where ω is the radiation angular frequency, ν_ei is the collisional frequency (2.38) and ω_p is the frequency of electron plasma oscillations

$$\omega_\mathrm{p} = \frac{4\pi e^2 n_\mathrm{e}}{m_\mathrm{e}}. \tag{3.5}$$

Given the permittivity and assuming permeability $\mu \approx 1$, the refractive index is approximated as follows [9]

$$n = \mathrm{Re}\big(\sqrt{\mu\epsilon}\big) \approx \mathrm{Re}\big(\sqrt{\epsilon}\big). \tag{3.6}$$

3.3 Ray-tracing algorithm

The principle of the algorithm stems directly from the ray equation (3.1). It can be easily shown that for a constant n, the trajectory of a ray resulting from the ray equation is a straight line.

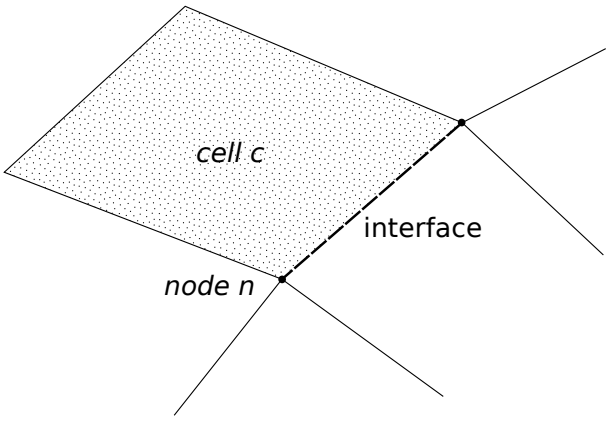

FIGURE 3.1: Representation of 2D domain decomposition into quadrilateral cells, nodes and interfaces between cells [6]

Moreover, using the ray equation on an interface of two environments with different constant indexes of refraction n_1, n_2, the well known Snells's law can be derived [9]

$$\sin\theta_1 n_1 = \sin\theta_2 n_2, \tag{3.7}$$

where θ_1 is the angle of incidence and θ_2 is the angle of refraction. Both angles are measured from the normal to the interface in the respective direction. As previously pointed out [6], from a computational point of view, it is rather advantageous to reformulate Snell's law in the following the vector form [19]

$$\mathbf{d_2} = \frac{n_1}{n_2}\mathbf{d_1} + \left(\frac{n_1}{n_2}\gamma - \sqrt{1 - \left(\frac{n_1}{n_2}\right)^2 (1-\gamma^2)}\right)\mathbf{n}, \tag{3.8}$$

where

$$\mathbf{n} = \begin{cases} \mathbf{n}_1, & \text{if } -\mathbf{n_1}\cdot\mathbf{d_1} > 0 \\ \mathbf{n}_2 & \text{otherwise,} \end{cases} \tag{3.9}$$

$$\gamma = -\mathbf{n}\cdot\mathbf{d}_1. \tag{3.10}$$

Here, $\mathbf{n_1}$ and $\mathbf{n}_2$ are normal unit vectors to the interface with opposite directions, $\mathbf{d}_1$ is the unit vector in the direction of incidence and $\mathbf{d}_2$ is the unit vector of the ray direction after refraction.

The algorithm then relies on a decomposition of the computational domain into cells with constant values of thermodynamic variables, as schematically shown for a 2D domain in Figure 3.1. In finite difference schemes, the procedure is straightforward as the domain is naturally divided into cells with straight boundaries. To obtain such zones in the finite element problem formulated in chapter 2, the 0th order elements in $L_2(\Omega(t))$

and 1st order elements in $\left[H^1(\Omega(t)\right]^d$ are necessary. In 2D triangular or quadrilateral cells are usually used both having its advantages and disadvantages. Hydrodynamic code PETE2 [12] is written with quadrilateral cells in mind, leading to the usage of quadrilateral cells throughout this work, except for a simple test case in section 3.4.

The choice of finite elements significantly limits the advantages the finite element method over a finite difference scheme. A possible solution is to use the finite elements of an arbitrary order to perform the hydrodynamic part of the simulation and then project the appropriate variables to a much finer mesh of the 0th order, respectively 1st order elements. This ensures that a high order of accuracy is maintained throughout the simulation and enables more flexibility in terms of elements geometry. This work paves the way to this projection by implementing the algorithm for low order elements in a finite elements hydrodynamic code.

We already fully described the implementation of the ray tracing algorithm in [6]. To summarize, finding a trajectory of a ray in a decomposed computational domain is performed in the following steps:

1. An intersection of the ray with the domain boundary is found.
2. A cell adjacent to the intersection is found and the ray is propagated as a straight line throughout the cell. A new intersection at the interface on the opposite side of the cell is found.
3. In this point, electron density gradient is calculated using linear interpolation from nodes. Calculation of nodal gradient is described in chapter 6.
4. Snell's law is used to determine the new direction of the ray. Here, the **electron density gradient is used instead of the normal unit vector to the face**. This is a key part of the algorithm and motivates the study of gradient calculation methods.
5. The new cell, adjacent to the interface, is chosen based on the direction and the algorithm either stops if a domain boundary is reached or returns to step 2.

3.4 Integral solution of the ray equation

To obtain a reference solution of the ray equation, a special coordinate system, density profile, and index of refraction model are specified. This is done in such a way that the ray equation reduces to a simple set of ordinary differential equations that can be numerically integrated using a high-order integration method.

A combination of coordinates (θ, ϕ, n) originally described in [9] and Cartesian coordinates is used. Using standard xyz Cartesian coordinates, θ is the angle between the z-axis and the ray, ϕ is the angle between the ray and x-axis in the xy plane. This leads to the following form of directional derivative along the ray [9]

$$\frac{\mathrm{d}}{\mathrm{d}s} = \frac{\mathrm{d}\theta}{\mathrm{d}s}\frac{\partial}{\partial\theta} + \frac{\mathrm{d}\phi}{\mathrm{d}s}\frac{\partial}{\partial\phi} + \frac{\mathrm{d}n}{\mathrm{d}s}\frac{\partial}{\partial n}. \tag{3.11}$$

As has been previously shown in [9][6], this leads to a system of ordinary differential equations. The system is further simplified by looking for a solution in the yz plane only and thus eliminating ϕ from the equations. The final form of the ordinary differential equations is

$$\frac{\mathrm{d}}{\mathrm{d}s}\begin{pmatrix} y \\ z \\ \theta \end{pmatrix} = \begin{pmatrix} \sin\theta \\ \cos\theta \\ \frac{1}{n}\left(\cos\theta\frac{\partial n}{\partial y} - \sin\theta\frac{\partial n}{\partial z}\right) \end{pmatrix} \tag{3.12}$$

At this point the special setting of electron density profile and index of refraction model plays a major role. Considering the density profile to be [6]

$$n_\mathrm{e} = n_\mathrm{e}^\mathrm{crit}\left(1 - z^2\right) \tag{3.13}$$

and using the model of index of refraction

$$n = \sqrt{1 - \frac{n_\mathrm{e}}{n_\mathrm{e}^\mathrm{crit}}} \tag{3.14}$$

the resulting profile of index of refraction is simply

$$n = \pm|z|. \tag{3.15}$$

The reason to also specify a density profile, and not directly the index of refraction profile, is to properly test the implementation of the method as the algorithm takes n_e as an input variable and calculates the index of refraction based on model (3.4). By setting the collision frequency to 0 in (3.4) the simplified model (3.14) is obtained and no special case needs to be treated in the code.

The direct integration was performed in [6] for various initial conditions $(y, z, \theta) = (0.01, -1, \theta_0)$, where θ_0 is 0.1, 0.2, 0.25 and 0.5 on a randomly perturbed triangular mesh with total of 400 cells. It was compared with results obtained by using the algorithm described in section 3.3. The comparison is shown in Figure 3.2 for θ_0 0.1 and 0.2 and in Figure 3.3 for θ_0 0.25 and 0.5.

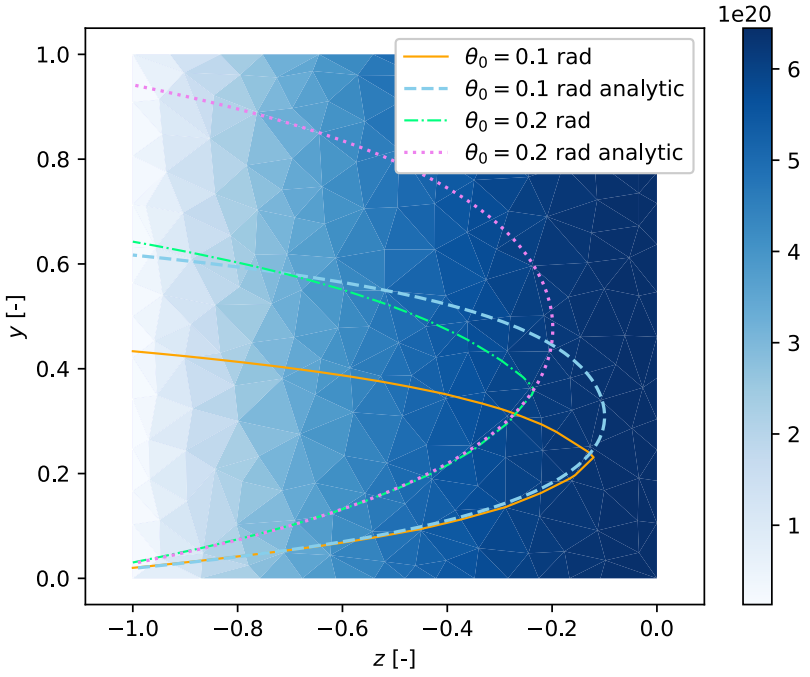

FIGURE 3.2: Ray tracing compared with direct integration for initial angle of incidence θ_0 equal to 0.1 and 0.2 rad on a randomly perturbed triangular mesh with total of 400 cells [6]

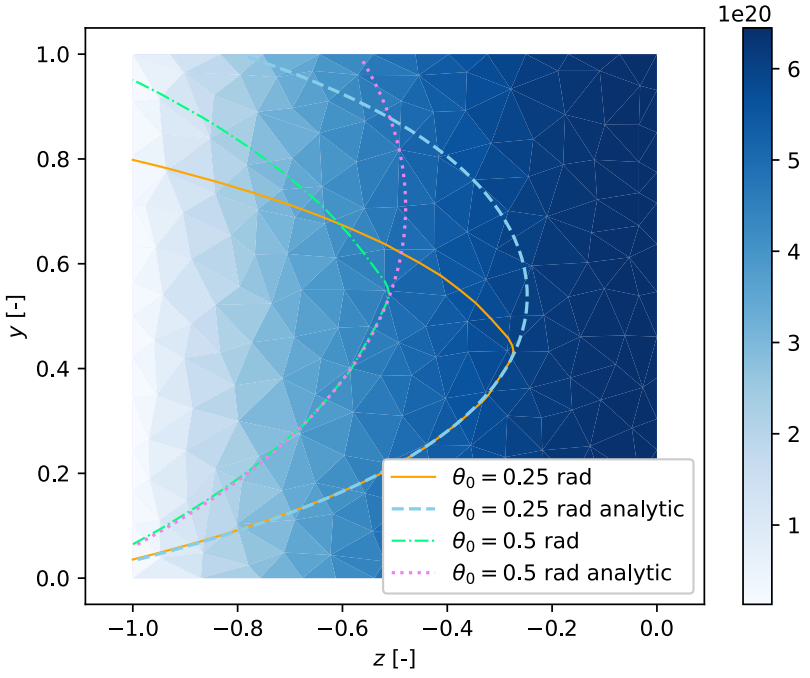

FIGURE 3.3: Ray tracing compared with direct integration for initial angle of incidence θ_0 equal to 0.25 and 0.5 rad on a randomly perturbed triangular mesh with total of 400 cells [6]

We already analyzed the results in [6] and we have drawn the following conclusions: "It can be seen that the ray-tracing follows the directly integrated solution until a near effective critical density given by

$$n_{\mathrm{e}}(z_{\mathrm{t}}) = n_{\mathrm{e}}^{\mathrm{crit}}(2\sin\theta_0 - \sin^2\theta_0). \tag{3.16}$$

at position

$$z_{\mathrm{t}} = 1 - \sin\theta_0, \tag{3.17}$$

is reached. Here, the conditions for total reflection given by negative radicand in equation (3.8) are met and the ray makes a sharp turn. This is a known effect of this type of method. The results are similar to those in [9].".

3.5 Special case analytic solutions of the eikonal equation

It turns out that the eikonal equation (3.2) can be reformulated in such a way that its analytic solutions are apparent for particular profiles of index of refraction [8]. Eikonal defined in (3.3) is related to the local wave vector by $\mathbf{k} = \omega\boldsymbol{\nabla}S$ [8]. The group velocity of the radiation can then be expressed using the eikonal

$$\mathbf{v}_{\mathrm{g}} = \frac{\partial\omega}{\partial\mathbf{k}} = c\boldsymbol{\nabla}S. \tag{3.18}$$

By differentiating the group velocity with respect to time and using the equations (3.2), (3.18) a new equation [8]

$$\frac{\mathrm{d}\mathbf{v}_g}{\mathrm{d}t} = \frac{\mathrm{d}\boldsymbol{\nabla}S}{\mathrm{d}t} = c\big(\mathbf{v}_g\cdot\boldsymbol{\nabla}\big)(\boldsymbol{\nabla}S) = c^2(\boldsymbol{\nabla}S\cdot\boldsymbol{\nabla})(\boldsymbol{\nabla}S) = \frac{c^2}{2}\boldsymbol{\nabla}\Big(|\boldsymbol{\nabla}S|^2\Big) = \boldsymbol{\nabla}\left(\frac{c^2}{2}n^2\right) \tag{3.19}$$

is obtained. This equation is called the equation of motion of a ray as it has the same form as an equation of motion for a unit mass particle in potential $-\frac{c^2}{2}n^2$ and directly describes the trajectory of the ray in relation to n

$$\frac{\mathrm{d}^2\mathbf{r}}{\mathrm{d}t^2} = \boldsymbol{\nabla}\left(\frac{c^2}{2}n^2\right). \tag{3.20}$$

Solutions for a particular right-hand sides of this equation are very well known. Two of them are demonstrated here.

3.5.1 Analytic ray trajectory in a constant electron density gradient

Using the equation (3.14) for the index of refraction, the equation of motion of the ray reads

$$\frac{\mathrm{d}^2\mathbf{r}}{\mathrm{d}t^2} = -\frac{c^2}{2n_\mathrm{c}}\boldsymbol{\nabla} n_\mathrm{e}. \tag{3.21}$$

We will look for a trajectory of a ray initially propagating perpendicular to the gradient in the plane of propagation. We set the gradient to be in the x direction $\boldsymbol{\nabla} n_\mathrm{e} = (G_x, 0)$. Initial position of ray is (x_0, y_0) and initial velocity of the ray is $\mathbf{v}_0 = (0, v_{0y}) = (0, cn_0)$. Here n_0 is the initial index of refraction

$$n_0 = \sqrt{1 - \frac{n_{\mathrm{e}0}}{n_\mathrm{c}}}, \tag{3.22}$$

where $n_{\mathrm{e}0}$ is the initial electron density. We obtain two equations

$$\frac{\mathrm{d}^2\mathbf{x}}{\mathrm{d}t^2} = -\frac{c^2}{2n_\mathrm{c}}G_x, \tag{3.23}$$

$$\frac{\mathrm{d}^2\mathbf{y}}{\mathrm{d}t^2} = 0. \tag{3.24}$$

The equations are solved by integration from the initial conditions. After eliminating time from the solution, we obtain the trajectory of the ray

$$x(y) = x_0 - \frac{G_x}{4(n_c - n_{\mathrm{e}0})}(y - y_0)^2. \tag{3.25}$$

It can be recognized that (3.25) describes a parabola.

3.5.2 Analytic ray trajectory in a quadratic electron density

A linear index of refraction is obtained in the case of a quadratic density gradient. Substituting in (3.15) and looking for a solution for $z < 0$ leads to a quadratic potential and nontrivial equation for $z(t)$

$$\frac{\mathrm{d}^2 z}{\mathrm{d}t^2} = -c^2 z. \tag{3.26}$$

The minus sign originates from the fact that the index of refraction is in this case a decreasing function of z. The solution is given by

$$z(t) = A\cos\left(\tilde{B}t\right), \tag{3.27}$$

where the constants A and B are determined from the initial conditions. As the equations for other coordinates have zero right hand side, the solution for y is $y(t) = \tilde{C}t + D$. For

particular initial conditions the solution is in the yz plane. The trajectory is then

$$z = A\cos(By + C), \tag{3.28}$$

where the constants A, B, C are determined from the initial conditions.

Chapter 4

Absorption models to simulate laser-plasma interaction

In the previous chapter, the geometric optics approximation is introduced and the procedure for finding the ray trajectories is discussed. But this is not the whole picture of plasma-laser interaction. For the algorithm to be useful, a model of the radiation power exchange with the plasma needs to be specified. To simulate a laser in a single time step of the simulation, a finite number of rays is constructed an appropriate power is assigned to each of them. The power exchange is then calculated for each of the rays independently. This chapter describes the models and approximations used to simulate the power exchange.

4.1 Associating power to the rays

The goal of this chapter is to describe the source term $-\boldsymbol{\nabla} \cdot \mathbf{S}$ in the equation (2.6). Similar to the heat transfer model described in section 2.3, an operator splitting technique [7] is employed. The exchange of power with the laser is evaluated solving only the equation

$$\rho c_{\mathrm{Ve}} \frac{\mathrm{d}T_{\mathrm{e}}}{\mathrm{d}t} = -\boldsymbol{\nabla} \cdot \mathbf{S}. \tag{4.1}$$

Instead of formulating the problem in the framework of the finite element method, the right-hand side is directly approximated in the mesh cells via ray-tracing.

Usually, the laser is described in terms of its intensity and direction (or it is possible to obtain such description). We need to approximate the energy flux entering each of the cells of the discretized domain. As the flux is needed, it is sufficient to associate power to each of the rays.

To obtain the initial condition, it is assumed that the laser source is bounded in space. In 3D, this means the source is a finite area and in 2D the source is a line segment. The source is then covered by a set of rays. At any given time, each ray r covers a finite area Δa_r and the associated power is

$$P_r(t) = \int_{\Delta a_r} I(\mathbf{r}, t) \mathrm{d}\mathbf{r}. \tag{4.2}$$

In practice, it is assumed (although not necessary) that the laser intensity can be separated into a spatial and temporal profile

$$I(\mathbf{r}, t) = I_t(t) I_{\mathbf{r}}(\mathbf{r}). \tag{4.3}$$

The time profile is usually the Gaussian function specified by Δ^t_{FWHM}, time of arrival t_0 and maximum intensity $I_{\max}$

$$I_t(t) = I_{\max} \exp\left(-4 \ln(2) \frac{(t - t_0)^2}{\left(\Delta^t_{\mathrm{FWHM}}\right)^2} \right), \tag{4.4}$$

Spatial profiles used throughout this work are Gaussian or super-Gaussian. As the simulations are performed in 2D, a one dimensional function over the laser source line segment must be specified. Let x denote the coordinate on the line segment. Then the super-Gaussian function has the following form

$$I_{\mathbf{r}}(\mathbf{r}) = I_x(x) = \exp\left(-\left(\frac{(x - x_0)^2}{2\sigma^2} \right)^P \right), \tag{4.5}$$

where x_0 is the position of maxima, P is the super-Gaussian exponent and σ^2 is its variance, which can be expressed in terms of $\Delta^{\mathrm{s}}_{\mathrm{FWHM}}$ as

$$\sigma^2 = \frac{\left(\Delta^{\mathrm{s}}_{\mathrm{FWHM}}\right)^2}{8(\ln 2)^{\frac{1}{P}}}. \tag{4.6}$$

The spatial integration is performed numerically by the trapezoidal rule.

4.2 Model of absorption via inverse bremsstrahlung

An effect contributing the most to the energy exchange is inverse bremsstrahlung. We already described the process in [6] and the model is taken from [9]. In summary, bremsstrahlung is a process through which electrons emit radiation when deflected by ions (the word originates from German and means braking radiation). The inverse

process to this is called inverse bremsstrahlung and describes an electron absorbing a radiation photon.

First, the radiation transfer equation [1] is taken, to estimate the effect of bremsstrahlung

$$\frac{\mathrm{d}I(\mathbf{r},t)}{\mathrm{d}s} = j(\mathbf{r},t) - k(\mathbf{r},t)I(\mathbf{r},t), \tag{4.7}$$

where j is the so-called emissivity coefficient, k is an absorption coefficient of the media and s is a parameter in the direction of Poynting vector of the radiation. First, we neglect emissivity, as we are interested in modeling an absorption process. A solution for a single cell with a constant values of the thermodynamic quantities is sought, thus, a constant value of the absorption coefficient is assumed. To obtain an equation for power P_r, of the ray r, we integrate over the ray area Δa_r, perpendicular to the ray trajectory

$$\int_{\Delta a_r} \frac{\mathrm{d}I(s,x_\mathrm{p},y_\mathrm{p},t)}{\mathrm{d}s}\mathrm{d}x_p\mathrm{d}y_p = -\int_{\Delta a_r} kI(s,x_\mathrm{p},y_\mathrm{p},t)\mathrm{d}x_p\mathrm{d}y_p, \tag{4.8}$$

$$\frac{\mathrm{d}P_r(s,t)}{\mathrm{d}s} = -kP_r(s,t). \tag{4.9}$$

The total power deposited $\Delta P_r = (-\boldsymbol{\nabla}\cdot\mathbf{S})_c$ by a single ray in the cell c is obtained by integrating over the parameter s in the cell

$$(-\boldsymbol{\nabla}\cdot\mathbf{S})_c = P_r^{\mathrm{in}}(1-\exp(kl)). \tag{4.10}$$

Here, l is the distance traveled by the ray r in the cell c and P_r^{in} is the power of the ray when entering the cell.

Finally, the relation from [9] for bremsstrahlung absorption coefficient $k = k_{\mathrm{ib}}$ is used

$$k_{\mathrm{ib}} = \frac{2\omega}{c}\,\mathrm{Im}\{\sqrt{\varepsilon}\}, \tag{4.11}$$

where ε is the permitivity (3.4).

4.3 Resonant absorption model

An important effect, attributed to the wave nature of the radiation, is a resonance near critical density. The effect is maximal for a p-polarized wave. The p-polarization means the radiation is polarized parallel to the plane of incidence. On the other hand, s-polarization is the term for radiation polarized perpendicular to the plane of incidence and no resonance is present in that case [20].

A model estimating the power exchange is originally developed in [20]. We implemented this model in [6] using assumptions from [9]. The model is used when a total reflection occurs (the radicand is negative in (3.8)). The power exchange is estimated based on the resonance of the wave over a characteristic length L_{char}. The length is devised from the electron density gradient at the point of total reflection $|\boldsymbol{\nabla} n_{\text{e}}|^{\text{crit}}$ and the model [20] estimates that the exchanged power of the ray r is absorbed in the cell c, through which the ray passes before reflecting

$$(-\boldsymbol{\nabla}\cdot\mathbf{S})_c = aP_r^{\text{in}}, \quad a = 18q\frac{\text{Ai}^3(q)}{|\text{Ai}'(q)|}, \tag{4.12}$$

$$q = \left(\frac{\omega}{c}L_{\text{char}}\right)^{\frac{2}{3}}\left(1-(\mathbf{d}_1\cdot\mathbf{n})^2\right), \tag{4.13}$$

$$L_{\text{char}} = \frac{n_{\text{e}}^{\text{crit}}}{|\boldsymbol{\nabla} n_{\text{e}}|^{\text{crit}}}, \quad n_{\text{e}}^{\text{crit}} = \frac{m_{\text{e}}\omega^2}{4\pi e^2}. \tag{4.14}$$

Here, Ai is the Airy function, d_1 is the unit direction of the incident ray, and $\mathbf{n}$ is the normal to the interface as defined by (3.9). Here, it should be emphasized that $\mathbf{n}$ is obtained from the electron density gradient, instead of the unit vector in the direction of normal to the interface, as was already pointed out in section 3.3.

To avoid the computationally intensive evaluation of the Airy function an approximate relation for the coefficient a introduced in [9] is used

$$a = \frac{\pi}{2}q\frac{\exp\left(-\frac{4}{3}q^{\frac{3}{2}}\right)}{q+0.48} \tag{4.15}$$

4.4 Model of absorption based on Fresnel equations

Another model applied in this work is based on the Fresnel equations at an interface of two different optical media. The Snells's law (3.8) for a perpendicular incidence of ray ($\gamma = 1$) never produces a negative radicand even for index of refraction n_2 close to zero and thus the total reflection is never triggered. In reality, there is always a refracted and reflected part of the radiation until the conditions are met for the total reflection. In ray-tracing, it is assumed that the reflection is negligible and that most of the power is carried by the refracted ray. Thus, only the refracted ray is followed. This may lead to a ray penetrating through a critical density and propagating into the region, where no radiation is present, as it is already absorbed or reflected in reality. This is a concern mainly at the beginning of the simulation, where the irradiation is nearly perpendicular and the density profile is steep.

To address the issue, there is another numerical condition implemented that triggers the ray reflection if it crosses a cell with electron density n_e higher than $n_\mathrm{e}^\mathrm{crit}$ defined in (4.14) and the Fresnel model of absorption is employed.

The Fresnel equations determine the ratio between electric amplitudes of the refracted and reflected waves [17] and consequently the amount of power reflected by squaring the electric fields [18]. For s-polarization, the ratio of total power reflected is

$$R_\mathrm{s} = \left| \frac{n_1\gamma - n_2\sqrt{1 - \left(\frac{n_1}{n_2}\right)^2(1-\gamma^2)}}{n_1\gamma + n_2\sqrt{1 - \left(\frac{n_1}{n_2}\right)^2(1-\gamma^2)}} \right|^2 \tag{4.16}$$

and for p-polarization the ratio is

$$R_\mathrm{p} = \left| \frac{n_1\sqrt{1 - \left(\frac{n_1}{n_2}\right)^2(1-\gamma^2)} - n_2\gamma}{n_1\sqrt{1 - \left(\frac{n_1}{n_2}\right)^2(1-\gamma^2)} + n_2\gamma} \right|^2 . \tag{4.17}$$

The identical notation as in (3.8) is used. It is further assumed that when the model is triggered by the density condition, all the refracted power of the radiation is absorbed locally. For example, in the case of p polarization, the absorbed power of ray r in cell c, where the condition was triggered, is

$$(-\boldsymbol{\nabla}\cdot\mathbf{S})_c = (1 - R_\mathrm{p})P_r^\mathrm{in}. \tag{4.18}$$

Chapter 5

X-ray gain coefficient model

One of the goals of this work is to estimate the amplification of a seeding x-ray pulse propagating through a plasma created by a driving laser interacting with a solid target. The idea is to use the same developed ray-tracing algorithm for both, the simulation of the driver and the seed. To be able to simulate the seeding pulse power, we implemented a gain coefficient model [7], [6] that connects the thermodynamic quantities of the plasma to its lasing properties.

5.1 Description of the model

Similarly to the model of inverse bremsstrahlung, the radiation transfer equation (4.7) is taken as a starting point for the derivation. Following the same assumptions as in chapter 4, an equation (4.9) for ray power is obtained. The process of laser amplification increases the laser power. This is reflected in the equation by a negative absorption coefficient k. It is a common practice [1] to introduce a new coefficient

$$g = -k \tag{5.1}$$

called the gain coefficient. The equation for x-ray pulse power in a cell then has an analogous form to (4.9)

$$\frac{\mathrm{d}P_r(s,t)}{\mathrm{d}s} = gP_r(s,t). \tag{5.2}$$

Solving the equation, power radiated away by the plasma in the single ray r from the cell c is estimated

$$(\boldsymbol{\nabla}\cdot\mathbf{S})_c = P_r^{\mathrm{in}}(\exp(gl)-1). \tag{5.3}$$

The rest of this section summarizes the estimation of g based on thermodynamic variables of the plasma as developed in [6].

We are interested in the plasma lasing on a specific transition, identified as an optimal candidate for the maximal possible power gain values by [21], [10]

$$2p^5_{1/2}3s_{1/2}, J = 1 \longrightarrow 2p^5_{1/2}3p_{1/2}, J = 0 \tag{5.4}$$

in neon-like ions. These ions are present in the plasma created by the interaction of a laser with a solid target. Multiple options exist for the target material, for example, [21] studies germanium as a possibility. In contrast, following [10], this work is mostly interested in the use of iron target, although in general the model is material independent and a calculation in germanium is used to verify the model. The wavelength of the transition in iron is $\lambda = 25.5\,\mathrm{nm}$. The jj-coupling notation used in (5.4) follows [22].

The gain coefficient is calculated as [1]

$$g = \frac{\pi e^2}{c m_\mathrm{e}} g_1 f_{12} \left(\frac{N_2}{g_2} - \frac{N_1}{g_1} \right) \Phi(\nu). \tag{5.5}$$

Here, $g_1 f_{12}$ is product of the lower level degeneration and oscillator strength, it is usually called the weighted oscillator strength and treated as a single value. Fractions, $\frac{N_2}{g_2}$ and $\frac{N_1}{g_1}$ are population densities of the upper and lower levels and g_2, g_1 are the degenerations of the levels [22]. Level population density means density of ions with the electron configuration having specific energy. The function $\Phi(\nu)$ is a spectral line profile.

5.1.1 Spectral line broadening

A common simplifying assumption is that the spectral line profile is a rectangular function [1]

$$\Phi(\nu) = \Phi = \frac{1}{\Delta\nu}, \tag{5.6}$$

where $\Delta\nu$ is the width of the spectral line.

A line broadening due to two effects is taken into account. First, the Doppler broadening is estimated. The spectral lines broaden due to the fact that the plasma has non-zero temperature and the ions are moving with the thermal velocity. Relative to an observer, the motion towards or away results in a Doppler blue or redshift. The total Doppler line broadening is estimated to have a gaussian profile with FWHM [1]

$$\Delta\nu^\mathrm{D}_\mathrm{FWHM} = \frac{1}{2\sqrt{\ln 2}} \nu \sqrt{\frac{2k_\mathrm{b}T_\mathrm{i}}{m_\mathrm{u}c^2}}, \tag{5.7}$$

where T_i is the ion temperature.

The second effect taken into account is the broadening due to collisions. If an ion undertakes a collision just as it emits a photon, the process can be interrupted, effectively reducing the characteristic time of the process and thus increasing the uncertainty in energy. This leads to the line broadening characterized by a Lorentzian curve profile. The FWHM of this profile is estimated to be [1]

$$\Delta\nu^{\mathrm{L}}_{\mathrm{FWHM}} = \alpha n_\mathrm{e}^2 T_\mathrm{e}^{-1/2}. \tag{5.8}$$

Altogether, we assume that photons can be both Doppler shifted and collision shifted in the same frequency direction, leading to the following rectangular spectral line profile

$$\Phi(\nu) = \frac{1}{\Delta\nu^{\mathrm{D}}_{\mathrm{FWHM}} + \Delta\nu^{\mathrm{L}}_{\mathrm{FWHM}}}. \tag{5.9}$$

5.1.2 Population inversion and weighted oscillator strength

The weighted oscillator strength $g_1 f_{12}$ and level populations remain to be determined. A Flexible Atomic Code (FAC) [22] is used to perform the necessary calculations. The weighted oscillator strength of a transition can be directly measured, and is a tabulated value provided by the code for a given transition. A more complicated procedure based on solving a set of rate equations is needed to obtain an estimate of population inversion.

For an energy level l, the population and depopulation of the level occurs due to various physical processes. Using the same approximation as in the previous work [6], collisional excitation, collisional deexcitation and radiative deexcitation are assumed to be the dominant processes governing the population state. Other processes, such as, ionizing collisions, photo-recombination, photoexcitation, photoabsorption and three-body recombination are not included in the calculation. The level population N_l is then described by the the rate equation

$$\frac{\mathrm{d}N_l}{\mathrm{d}t} = \sum_{m>l} N_m A_{ml} - N_l \sum_{m<l} A_{lm} + \sum_m N_m C_{ml} - N_l \sum_m C_{lm}, \tag{5.10}$$

Radiative deexcitation from upper levels contributes by an increment governed by an Einstein coefficients A_{ml}. On the other hand, radiative deexcitation from level l to lower levels depopulates the level and is governed by the same Einstein coefficinet only evaluated for different transitions A_{lm}. The coefficient is represents the probability specific to each transition and is not a function of thermodynamic quatities. It can be tabulated and is provided by the FAC [22]. Similarly coefficients C_{lm}, C_{ml}, populate and depopulate the level through collisional excitation and deexcitation. These coefficients

are governed by the collisional cross-section $\langle \sigma_{lm} v \rangle$ and electron density [6]

$$C_{lm} = n_\mathrm{e} \langle \sigma_{lm} v \rangle. \tag{5.11}$$

Assuming a Maxwellian distribution of the velocities, the cross-section can be evaluated based on the electron temperature T_e [6].

Given M energy levels, a system of equations is obtained. The quasi-static approximation [1] is used to transform the system to a set of algebraic equations

$$\frac{\mathrm{d}N_l}{\mathrm{d}t} = 0, \quad i = 1, 2, \ldots, M. \tag{5.12}$$

Adding the condition on the total density of neon-like ions

$$N_1 + N_2 + \cdots + N_M = f_\mathrm{a} n_\mathrm{i}, \tag{5.13}$$

the system has a unique solution. Here f_a is the fraction of ions that are neon-like (fractional abundance) and n_i is the total ion density of the plasma.

Practically, calculating the values of Einstein coefficients is performed using the FAC [22]. The system of rate equations is formed and solved also by the FAC, which obtains the thermodynamic variables of the plasma as an input.

5.2 Verification of the model

In [23], the FAC was used to determine the relative energy level populations at $2p_{1/2}^5 3p_{1/2}$, $J = 0$ in neon-like germanium for electron densities ranging from $10^{20}\,\mathrm{cm}^{-3}$ to $10^{23}\,\mathrm{cm}^{-3}$ and electron temperatures 650 eV, 850 eV, …, 1850 eV. As the method of the populations calculation was the same as described in this work, it can be directly compared. This has been already done in the previous work [6]. The result is summarized here in Figure 5.1. Where the relative populations in neon-like germanium ions are shown as a function of electron density for various temperatures. The results are the same as in [23] and it can be concluded that the implementation of the energy level population calculation is correct.

5.3 Predictions of the model

In principle, the gain coefficient model can be thought of as a function of two variables, temperature T and electron density n_e. This is a simplification because the model

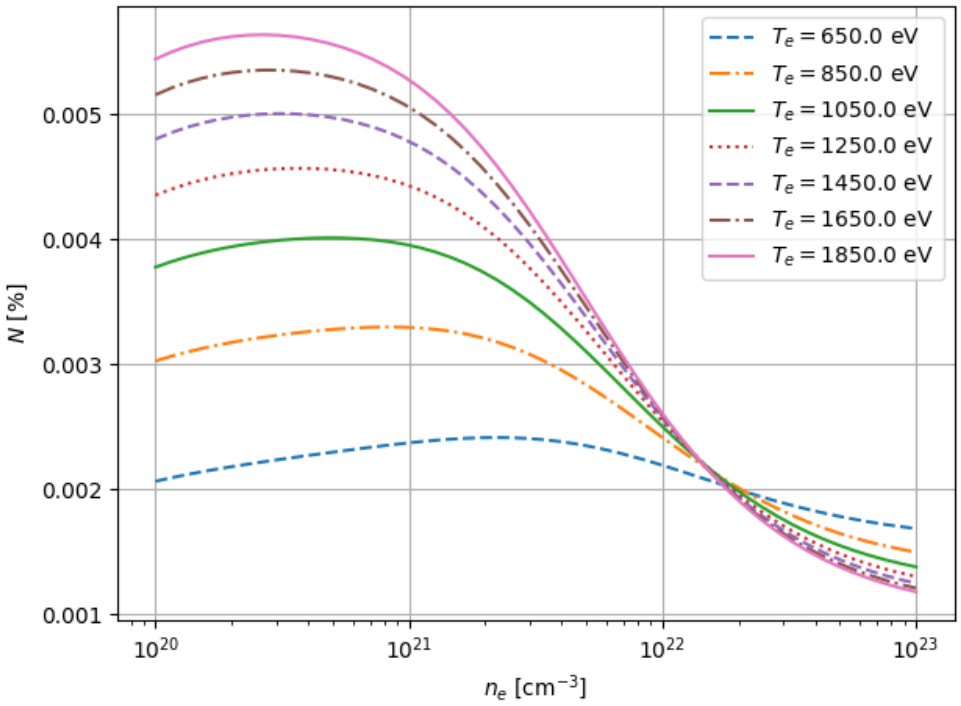

FIGURE 5.1: Relative populations N of $2p^5_{1/2}3p_{1/2}, J = 0$ in neon-like germanium at various temperatures T_e as a function electron density n_e [6]

actually uses two temperatures, the electron temperature T_e and ion temperature T_i. For sake of plotting the gain coefficient as a function of two variables, the temperatures are set equal to the one temperature T. Furthermore, the ion density n_i is also needed, but it can be easily calculated following the fact that we are dealing with neon-like ions in quasi-neutral plasma.

We calculated the gain coefficient using the transition of interest (5.4) in the previous work [6] for n_e ranging from $10^{19}\,\mathrm{cm}^{-3}$ to $10^{23}\,\mathrm{cm}^{-3}$ and T between 100 eV and 850 eV. The result is depicted in Figure 5.2

As already stated in [6], the gain coefficient maximum is around $9\,\mathrm{cm}^{-1}$ for $n_\mathrm{e} = 7.5 \times 10^{20}\,\mathrm{cm}^{-3}$ and $T = 421\,\mathrm{eV}$. The fact that there is an optimal value is supported by the observation, that with temperature rising over a certain threshold, the abundance of neon-like ions decreases. There is also an optimal range of densities where the collisional excitation and collisional deexcitation is just right for the inversion of the population to exist. This is shown in Figure 5.3, where the relative populations of the upper and lower levels as a function of n_e at optimal $T = 421\,\mathrm{eV}$ are shown.

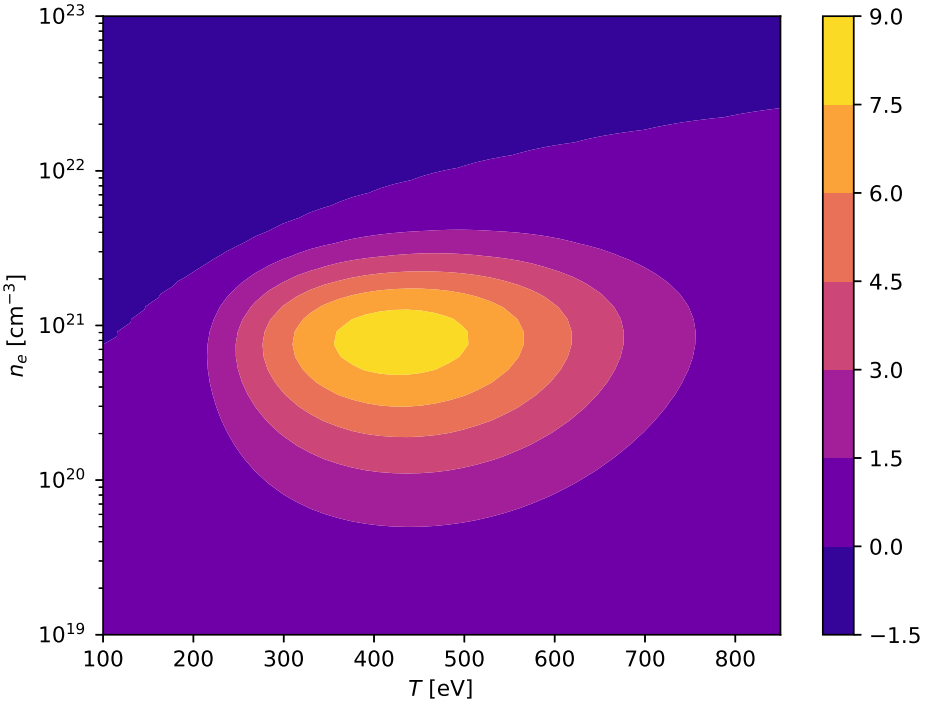

FIGURE 5.2: Gain coefficient as a function of temperature T and electron density n_e originally calculated in [6]

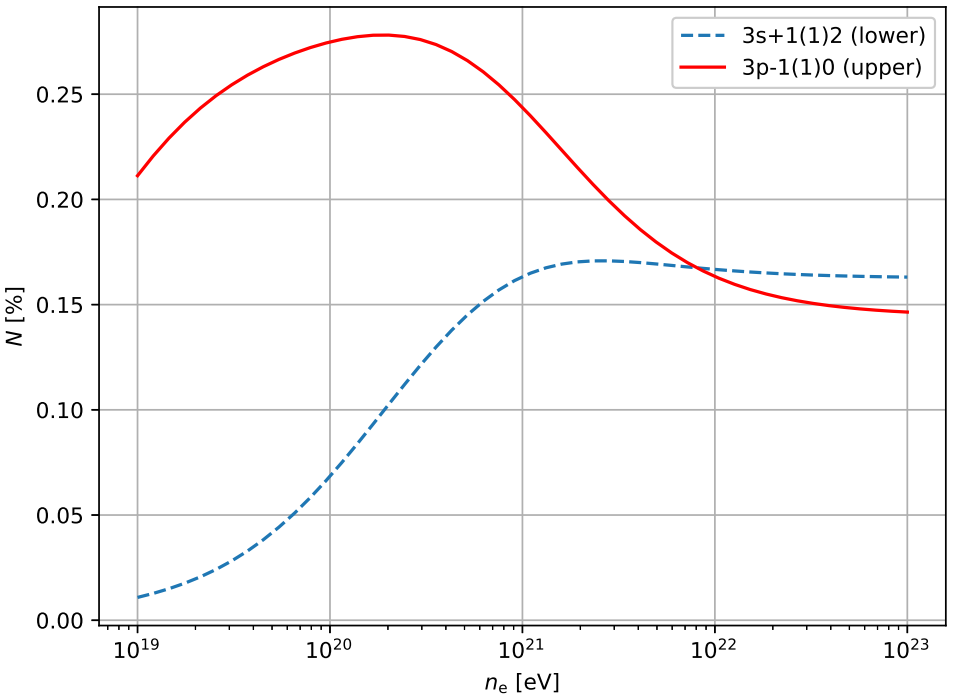

FIGURE 5.3: Population at the upper and lower energy levels as a function of n_e at $T = 421\,\text{eV}$ [6]

Chapter 6

Gradient calculation methods

In this chapter, three distinct methods of gradient calculation are presented. Furthermore, a simple problem with a known analytic solution is devised and the convergence of the introduced methods is studied.

A gradient at a specific point at an interface of two cells is required for the ray-tracing algorithm. A linear interpolation is used to obtain the gradient at this point using a gradient calculated in nodes. This approach is better than calculating the gradient in cells, where a discontinuity in the gradient at the interface arises. Thus, the goal of the methods is to calculate the gradient at nodal points of the mesh.

The first method, which uses Green's theorem over an appropriate stencil, is taken from [24]. The second method is based on a finite element formulation of the problem and the third method utilizes the least-squares formulation presented in [25].

6.1 Method using the Green's theorem

The equations taken from [24] for the first partial derivative of a function u are used. This corresponds to the method of the support operators for cell-valued scalar functions and node-valued vector functions. It is a direct consequence of the Green's theorem applied to the scalar function $u(x, y)$ that

$$\frac{\partial u}{\partial x} = \lim_{S \to 0} \frac{\oint_{\partial S} u \mathrm{d}y}{S}, \tag{6.1}$$

$$\frac{\partial u}{\partial y} = -\lim_{S \to 0} \frac{\oint_{\partial S} u \mathrm{d}x}{S}, \tag{6.2}$$

where S is a given region and ∂S its boundary.

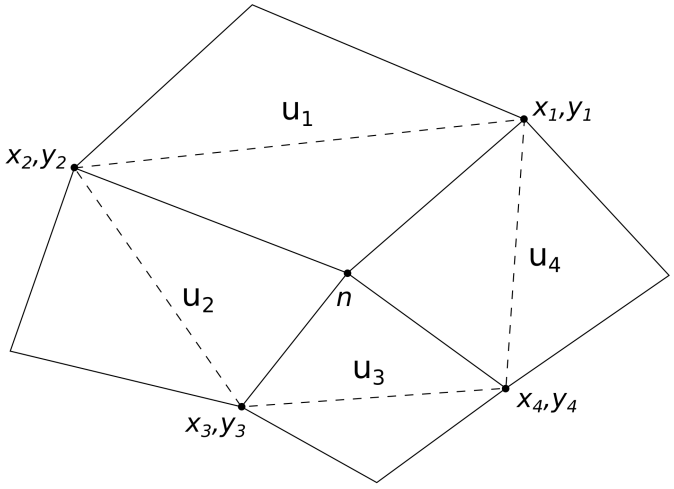

FIGURE 6.1: Integration stencil for gradient calculation using Green's formula

In the case of u defined in cells, S can be chosen in such a way that the integrals on the right-hand side of (6.1), (6.2) can be evaluated. The task is to evaluate the gradient at the node denoted by lower index n. The discrete stencil depicted in Figure 6.1 connecting the adjacent nodes is considered. Therefore, ∂S is a union of four sides. Furthermore, the value of function u is constant along these sides and corresponds to the cell values of the function. Also, the normal direction to each of the sides can be simply analytically evaluated. Using these considerations, a discrete formula for the nodal gradient is obtained. See [24] for detailed derivation.

$$\begin{aligned}(\boldsymbol{\nabla} u)_x\Big|_n =& \Big((y_2 - y_1)u_1 + (y_3 - y_2)u_2 + \\ &+ (y_4 - y_3)u_3 + (y_1 - y_4)u_4\Big)\frac{1}{S_n} \qquad (6.3)\\ , (\boldsymbol{\nabla} u)_y\Big|_n =& -\Big((x_2 - x_1)u_1 + (x_3 - x_2)u_2 + \\ &+ (x_4 - x_3)u_3 + (x_1 - x_4)u_4\Big)\frac{1}{S_n}. \qquad (6.4)\end{aligned}$$

Here, $x_1 \dots x_4$ and $y_1 \dots y_4$ are the corresponding coordinates of the nodes neighbouring the node n and $u_1 \dots u_4$ are the values of the function u in the adjacent cells as shown in Figure 6.1.

The area S_n can be evaluated as a sum of areas of the four triangles formed by the stencil and the node n. This is the approach used in this work. Alternatively, it can be calculated as

$$S_n = \frac{1}{2}\frac{S_1 + S_2 + S_3 + S_4}{4}, \qquad (6.5)$$

where $S_1 \dot{S}_4$ are the areas of the adjacent cells. This is advantageous in case that the cell areas are already pre-computed during the simulation.

6.2 Method based on the finite element formulation

Within the finite element formulation, the goal is to find a function $\mathbf{G}$ such that

$$\mathbf{G} = \boldsymbol{\nabla} u, \tag{6.6}$$

where u is a given smooth scalar function. Using the notation introduced in section 2.1, the equation is multiplied by a function $\boldsymbol{\psi}^{(k)}$, integrated over the domain Ω and then Green's theorem is applied. Note that G_i, $\psi_i^{(k)}$ is the i-th component of $\mathbf{G}$, $\boldsymbol{\psi}^{(k)}$ respectively

$$\int_\Omega G_i \psi_i^{(k)} \mathrm{d}V = \int_\Omega \frac{\partial u}{\partial x_i} \psi_i^{(k)} \mathrm{d}V = -\int_\Omega u \frac{\partial \psi_i^{(k)}}{\partial x_i} \mathrm{d}V + \oint_{\partial\Omega} u \psi_i^{(k)} n_i \mathrm{d}S, \tag{6.7}$$

where $\partial\Omega$ is the domain boundary and n_i is the i-th component of the normal vector at $\partial\Omega$. For the finite element formulation expansions to the bases functions are made

$$G_i = \sum_j g^{(j)} \psi_i^{(j)} \text{ where } g_i^{(j)} \in \mathbb{R},\ \boldsymbol{\psi}^{(j)} \in \mathcal{V} \tag{6.8}$$

$$u = \sum_j r^{(j)} \varphi^{(j)} \text{ where } r^{(j)} \in \mathbb{R},\ \varphi^{(j)} \in \mathcal{E} \tag{6.9}$$

Note that variables associated with the concrete test function are denoted using an upper index (eg. the coefficient associated with a concrete test function in function expansion). Using the Einstein notation, the weak formulation reads

$$\sum_j g^{(j)} \int_\Omega \psi_i^{(j)} \psi_i^{(k)} \mathrm{d}V = -\sum_j r^{(j)} \int_\Omega \varphi^{(j)} \frac{\partial \psi_i^{(k)}}{\partial x_i} \mathrm{d}V + \sum_j r^{(j)} \int_{\partial\Omega} \varphi^{(j)} \psi_i^{(k)} n_i \mathrm{d}S \quad \forall k. \tag{6.10}$$

This, given the coefficients $r^{(j)}$, where $j \in 1 \dots N$, results in a linear system of N equations for the coefficients $g^{(j)}$

$$\mathbb{M}_{j,k} g^{(j)} = b^{(k)}, \tag{6.11}$$

where $\mathbb{M}_{j,k} = \int_\Omega \psi_i^{(j)} \psi_i^{(k)} \mathrm{d}V$ and $b^{(k)}$ is the right hand side of the equation (6.10). In practice the process of assembling $\mathbb{M}$ and b and finding the solution is performed using MFEM [13], a lightweight scalable library for finite element methods.

6.3 Method based on the least-squares formulation

As described in [25], consider the expansion of the function u around node n

$$u = u_n + \left.\frac{\partial u}{\partial x}\right|_n (x - x_n) + \left.\frac{\partial u}{\partial y}\right|_n (y - y_n), \tag{6.12}$$

where x_n and y_n are the coordinates of the node n. The values of u are defined in the cell centroids. Standard approach [26] is to perform the reconstruction is a cell, where the value u_n is known. Here we want to obtain the gradient in a node n.

To find the reconstruction in the node n a method from [25] is used. The equation (6.12) is evaluated in the centroid of one of the cells c adjacent to the node n. There are three unknowns: $\overline{u_n}$, $\left.\overline{\frac{\partial u}{\partial x}}\right|_n$ and $\left.\overline{\frac{\partial u}{\partial y}}\right|_n$. To evaluate the gradient at node n, at least three adjacent cells are necessary to form a system of equations. For exactly three adjacent cells, this is equivalent to defining a plane given the three values in adjacent cells centroids and finding its slope. More than three adjacent cells taken into account lead to an overdetermined system of equations that can be solved in the least-squares sense. Following [25], the weighted least squares formulation is used

$$\mathbb{A}\mathbf{x} = \mathbf{b} \tag{6.13}$$

$$\mathbb{A} = \begin{bmatrix} w_1 & w_1(x_1 - x_n) & w_1(y_1 - y_n) \\ \vdots & \vdots & \vdots \\ w_c & w_l(x_c - x_n) & w_l(y_c - y_n) \\ \vdots & \vdots & \vdots \\ w_N & w_N(x_N - x_n) & w_N(y_N - y_n) \end{bmatrix}, \mathbf{x} = \begin{pmatrix} \overline{u_n} \\ \overline{\frac{\partial u}{\partial x}} \\ \overline{\frac{\partial u}{\partial y}} \end{pmatrix}, \mathbf{b} = \begin{pmatrix} w_1 u_1 \\ \vdots \\ w_c u_c \\ \vdots \\ w_N u_N \end{pmatrix}, \tag{6.14}$$

where the weights w_c are chosen according to [25]

$$w_c = \frac{1}{\left((x_c - x_n)^2 + (y_c - y_n)^2\right)^{P/2}}. \tag{6.15}$$

The exponent $P = 0.25$ is used, following the original work [25]

The system is solved in two steps. First, a QR factorization of the matrix $\mathbb{A}$ is performed using the Householder transformation [27]

$$\mathbb{A} = \mathbb{Q}\mathbb{R}, \tag{6.16}$$

where $\mathbb{Q}$ is an orthogonal matrix ($\mathbb{Q}^{-1} = \mathbb{Q}^T$) and $\mathbb{R}$ is a right triangular matrix. As matrix $\mathbb{A}$ is not rectangular, matrix $\mathbb{R}$ has multiple fully zero rows

$$\mathbb{R} = \begin{bmatrix} \mathbb{R}_1 \\ 0 \end{bmatrix} \tag{6.17}$$

Then, to obtain the solution of the linear least squares problem, the following system is solved

$$\mathbb{R}_1 \mathbf{x} = \mathbf{q}_1, \tag{6.18}$$

where $\mathbf{q}_1$ are the corresponding rows from the right hand side formed by

$$\mathbb{Q}^T \mathbf{b} = \begin{pmatrix} \mathbf{q}_1 \\ \mathbf{q}_2 \end{pmatrix}. \tag{6.19}$$

6.4 Study of the convergence of the methods

To study convergence of the methods, various meshes are used. Any mesh used in this study is fully described by two parameters. First is the number of cells in each dimension N. This number is used to generate a square orthogonal mesh with the side length equal to 1 covering a domain $(0, 1) \times (0, 1)$, divided into $N \times N$ square cells. The mesh is then randomized according to what is here called the randomization factor f. Each inner node (meaning not a node on the boundary) of the mesh is moved according to a random displacement

$$(\Delta x, \Delta y) \in \left(U\left(-f\frac{1}{N}, f\frac{1}{N}\right), U\left(-f\frac{1}{N}, f\frac{1}{N}\right) \right), \tag{6.20}$$

where $U(a, b)$ symbolizes the uniform distribution over an interval (a, b). The set of meshes with $N = 8,\ 16,\ 32,\ \ldots,\ 512$ and $f = 0,\ 0.02,\ 0.04$ is used, resulting in 21 different meshes in total.

Two analytic functions with known gradients $\mathbf{g}_a$ are used to evaluate the convergence of the methods. First is a simple linear function

$$u(x, y) = 2x + 3y \tag{6.21}$$

$$\mathbf{g}_a(x, y) = (2, 3), \tag{6.22}$$

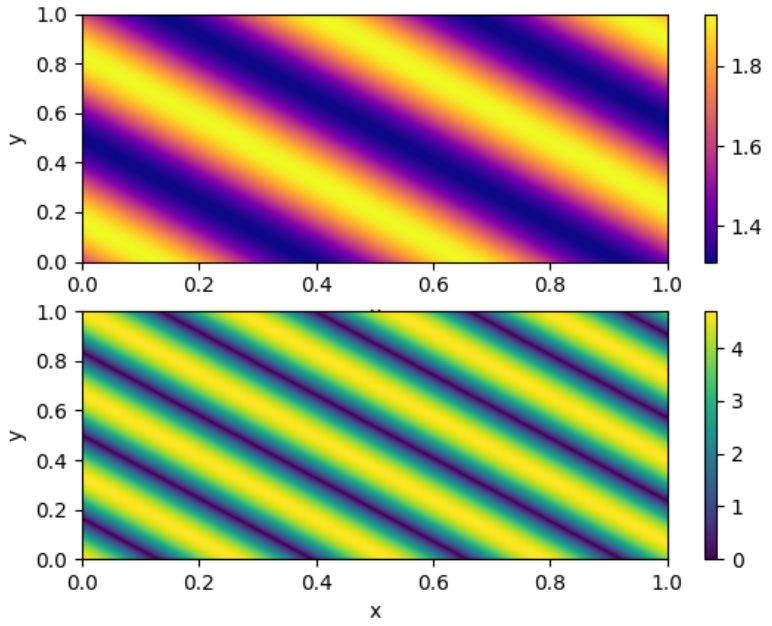

FIGURE 6.2: Analytic function used to evaluate methods convergence (top) and its gradient norm (bottom)

while the second is a smooth, non-linear function from [25]

$$u(x, y) = 1.62 + 0.31 \sin\big(\pi(3.79x + 2.98y)\big) \tag{6.23}$$

$$\mathbf{g}_a(x, y) = (1.1749\pi \cos\big(\pi(3.79x + 2.98y)\big), 0.9238\pi \cos\big(\pi(3.79x + 2.98y)\big)). \tag{6.24}$$

A graph of the latter function is in Figure 6.2.

For both of these functions, the procedure is identical. The function is projected to the cell centers of a chosen mesh using an integral projection procedure from the MFEM toolbox [13]. Then, one of the three described methods is used to calculate the gradient of the function. The difference between the analytic solution $\mathbf{g}_a$ and calculated solution $\boldsymbol{\nabla} u$ is processed in the following way

$$\Delta\varepsilon = \frac{\sqrt{\sum\limits_n S_n |\mathbf{g}_a - \boldsymbol{\nabla} u|^2}}{\sqrt{\sum\limits_n S_n |\mathbf{g}_a|^2}}, \tag{6.25}$$

where $\sum_n$ is sum over values in all nodes and S_n is an area associated to a given node n, calculated as the area of a polygon formed by adjacent cell centroids. The resulting number $\Delta\varepsilon$ is normalized discrete L_2 norm of the error in the vector size. The value of $\Delta\varepsilon$ is further referred to simply as the error for brevity.

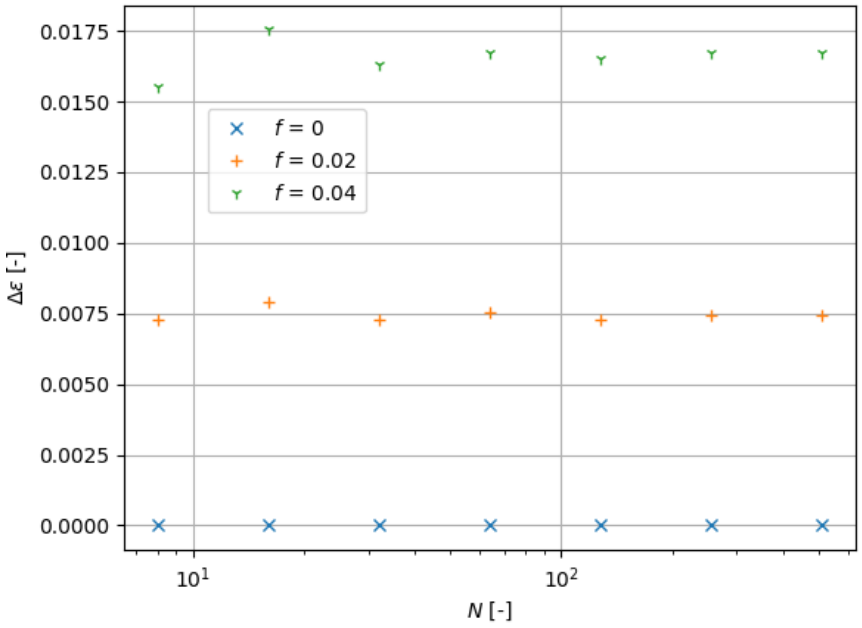

FIGURE 6.3: Error $\Delta\varepsilon$ as a function of the mesh segments count N and the randomization factor f for a linear function gradient, evaluated using the Green's formula method

6.4.1 Convergence of the method using the Green's theorem

First, Green's formula method was used to evaluate the error in a reconstruction of the linear function. For the sake of comparison with other methods, the gradient was evaluated at the inner nodes of the meshes. This is possible as a local reconstruction of the gradient is performed using this method. For practical usage of the method, boundary conditions would have to be specified for the problem.

The result for various various meshes are summarized in Figure 6.3. The method reconstructs the linear function exactly up to a round-off error for an orthogonal mesh. With increasing f, the value of $\Delta\varepsilon$ increases independently of N. This is well explained by the fact that [24] claims the method is of the zeroth-order truncation error $\mathcal{O}(1)$ on a general regular mesh and the second-order truncation error $\mathcal{O}(N^{-2})$ on a smooth mesh.

To further investigate the convergence, the method was used to evaluate a gradient of the sine function (6.23). The results are presented in Figure 6.4. It can be clearly seen that on a rectangular mesh ($f = 0$), the truncation error is indeed of second order. For the randomized meshes, the error reaches a threshold below which it no longer decreases with an increasing number of segments N. This also confirms the zeroth-order truncation error.

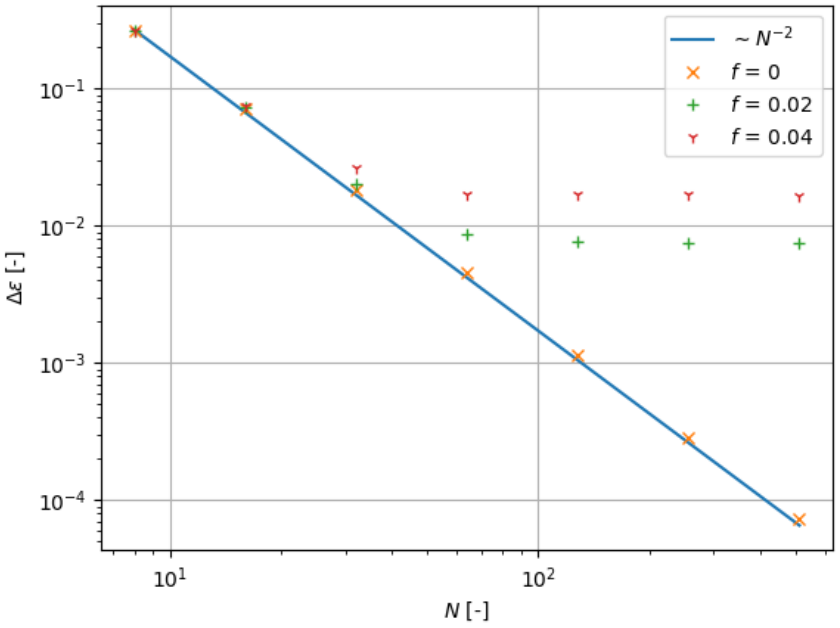

FIGURE 6.4: Error $\Delta\varepsilon$ as a function of the mesh segments count N and the randomization factor f for the sine function gradient, evaluated using the Green's formula method

6.4.2 Convergence of the method using the finite element formulation

Similarly to the case of Green's formula method, convergence of method using finite element formulation of the problem has been studied. To properly evaluate the gradient, essential boundary conditions [13] need to be specified. For sake of comparison, the boundary conditions are obtained by direct evaluation of the known analytical gradient.

First, the convergence was evaluated on the linear function (6.21). The result is depicted in Figure 6.5. The trend is remarkably similar to the errors obtained in the previous section, although the actual error values are higher. This method also reconstructs the linear function on an orthogonal grid down to a round-off error.

The resulting errors of gradient evaluation of the sine function (6.23) are shown in Figure 6.6. It can be seen that the error for various meshes depends on N analogously to the case of the Green's formula method in Figure 6.4. Second order convergence is observed only for the orthogonal mesh with $f = 0$.

6.4.3 Convergence of the method using the least-squares formulation

The results obtained using the least-squares formulation of the problem are processed in a similar fashion to the previous two methods. There is no need for a special treatment

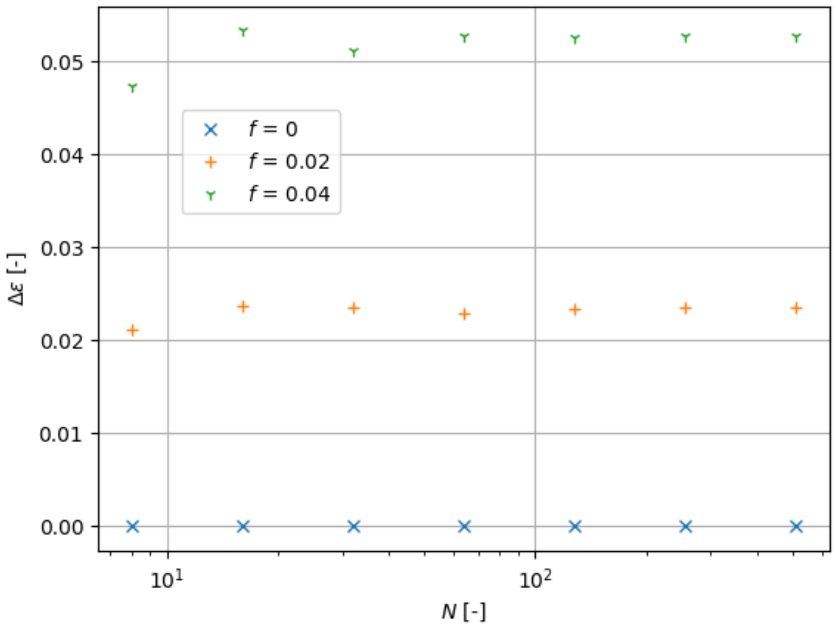

FIGURE 6.5: Error $\Delta\varepsilon$ as a function of the mesh segments count N and the randomization factor f for a linear function gradient, evaluated using the finite element formulation method.

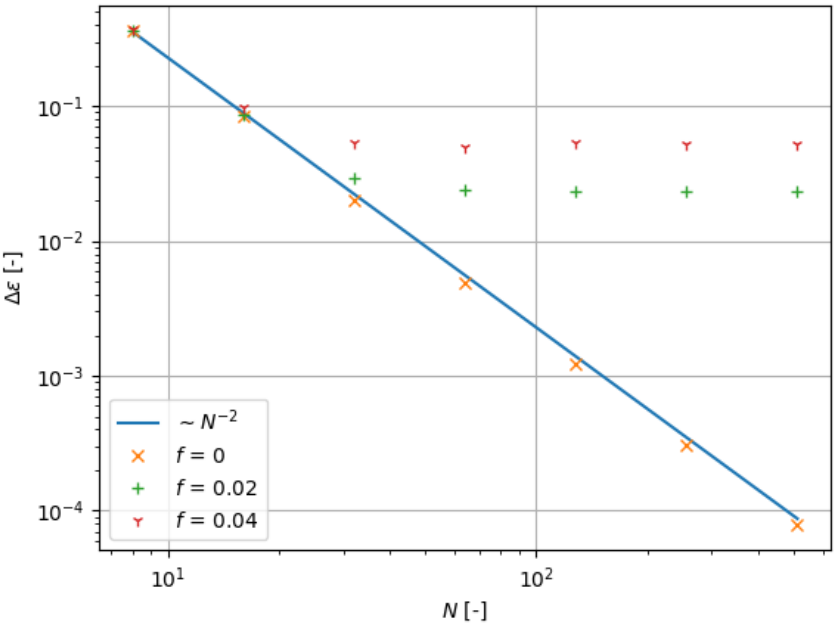

FIGURE 6.6: Error $\Delta\varepsilon$ as a function of the mesh segments count N and the randomization factor f for a sin function gradient, evaluated using the finite element formulation method.

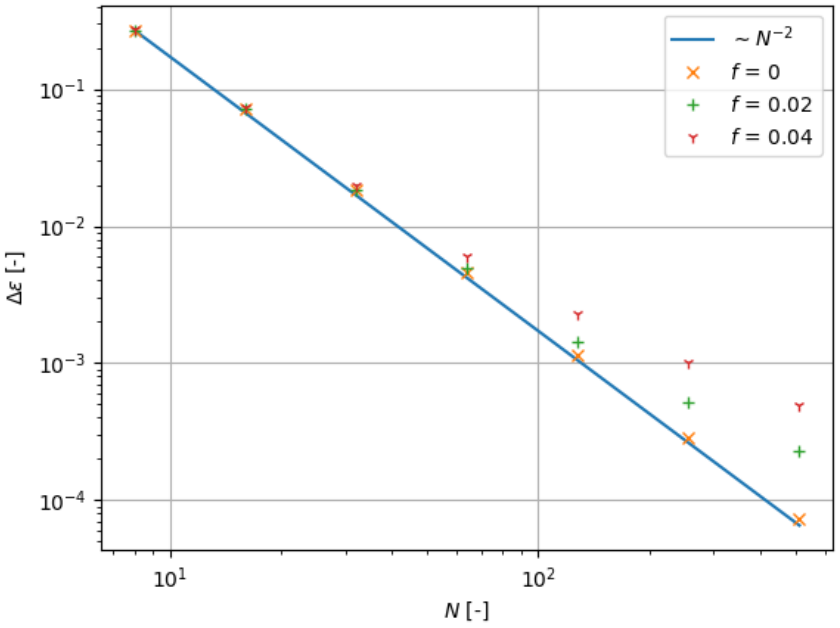

FIGURE 6.7: Error $\Delta\varepsilon$ as a function of the mesh segments count N and the randomization factor f for the sine function gradient, evaluated using the least-squares formulation of the problem.

of the boundary nodes as these can be ignored for the sake of comparison. This method reconstructs the gradient of the linear function up to a round-off error for all of the randomization factors f considered. Using the sine function, the relative error as a function of the number of segments for various randomization factors is summarized in Figure 6.7. It can be seen that the method shows close to second-order convergence even for an irregular grid.

6.5 Method imprinting into trajectory estimation

To determine how a chosen method influences the model of laser propagation, the following test case is proposed. It consists of a simulation with a parabolic profile of electron density and collisional frequency set to 0. In chapter 3, we have shown that in this case, an analytic solution to the ray trajectory can be found and that it is a cosine function. We use this fact to estimate the effects of the gradient calculation on accuracy of penetration depth. This test evaluates, how much does a choice of the method influences an absorption profile.

First, an analytic solution is constructed for a ray starting at the point $(0, 0)$ and with angle of incidence equal to 45°. A density profile is chosen based on critical density

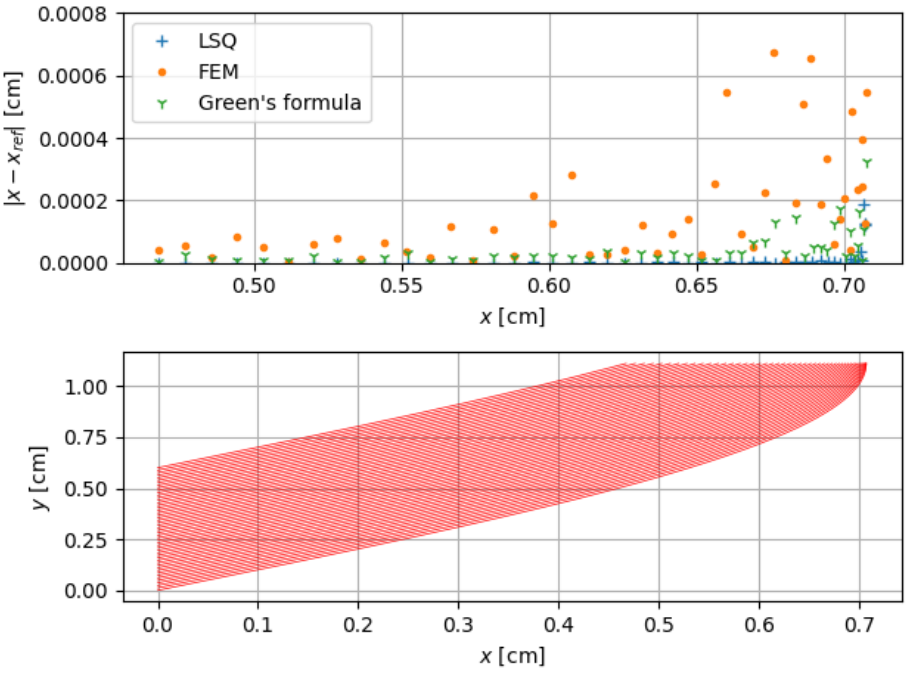

FIGURE 6.8: Rays propagating in a test case scenario in mesh with $N = 512$ and $f = 0$ (bottom) and a difference between the last intersection x coordinate and the depth of interpenetration computed analytically $|x - x_{\text{ref}}|$ for all three gradient calculation methods (top).

of radiation with wavelength of 25.5 nm.

$$n_{\text{e}}(x) = \frac{n_{\text{e}}^{\text{crit}}}{2}(1 + x^2). \tag{6.26}$$

The choice of wavelength is arbitrary and corresponds to the critical density $n_{\text{e}}^{\text{crit}} \doteq 1.71 \times 10^{24}\,\text{cm}^{-3}$. In this configuration, the analytic trajectory is

$$x(y) = n_{\text{e}}^{\text{eff}} \sin(\beta y), \quad \beta = \frac{n_{\text{e}}^{\text{crit}}}{2(n_{\text{e}}^{\text{crit}} - n_{\text{e}}^{\text{eff}})}, \tag{6.27}$$

where $n_{\text{e}}^{\text{eff}}$ is effective critical density (density evaluated at distance $\sin\theta_{\text{i}}$, where θ_{i} is the initial angle of incidence). In this case, it is n_{e} evaluated at $x = \frac{\sqrt{2}}{2}$. The turning point of the trajectory located at $y_{\text{t}} = \frac{\pi}{2\beta} \doteq 1.111$ is important, as the domain boundary is placed at this turning point.

In the described configuration, the rays are propagated using the ray-tracing algorithm with gradient calculated by one of the methods. At the point where it leaves the domain, its intersection can be directly compared with the analytic solution. This is performed not only for the ray originating from $(x_0, y_0) = (0, 0)$, but for a set of rays with the same angle of incidence but y_0 ranging from 0 to 0.6 cm. This is depicted in Figure 6.8 for one of the mesh configurations discussed further.

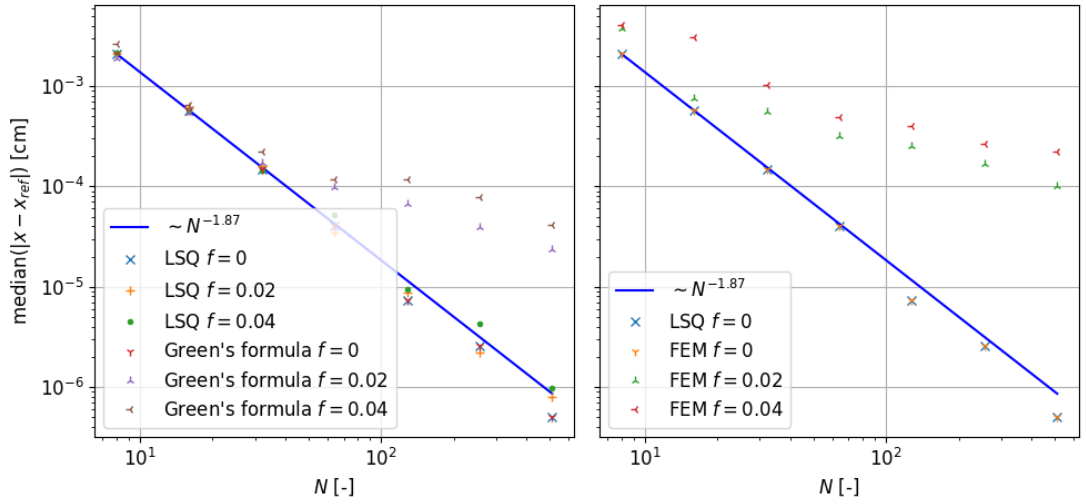

FIGURE 6.9: Median of the difference between the last intersection x coordinate and and the depth of interpenetration computed analytically median$|x - x_{\text{ref}}|$ over the 50 rays as a function of mesh configuration determined by N and f.

The whole procedure is repeated for 50 equidistant rays for all the mesh configurations described in section 6.4. To illustrate a single result, the ray trajectories and the resulting errors in their x coordinate of the final intersection are depicted in Figure 6.8 for mesh with $N = 512$ segments on one side and the randomization factor $f = 0$. It can be seen that the resulting absolute error $|x - x_{\text{ref}}|$ increases for rays ending closer to n_e^{eff}. This is an expected effect and has been pointed out in our previous work [6] and summarized here in Figure 3.2 and Figure 3.3.

To distinguish between the effect of the finite cell dimensions, leading to incorrect total reflection and the effect of error in the gradient calculation, the following statistical analysis is performed: a median and maximum of the errors over all 50 rays for each of the mesh configurations are taken. Comparison of median well describes the expected error introduced by the gradient calculation method while ignoring the extreme values resulting from the cell imprinting effects. On the other hand, the maximum characterizes the effects of finite cell dimensions.

A comparison of the median of the error as a function of mesh resolutions N and randomization factor f is shown in Figure 6.9 for all of the methods. It can be clearly seen that the same effects as when investigated in section 6.4 are present. While almost no dependence on f can be seen for rays propagating in density gradient calculated using the least-squares method (LSQ), the methods using the finite element formulation (FEM) and the Green's formula lead to an increased inaccuracy of the ray trajectory estimation on the distorted mesh.

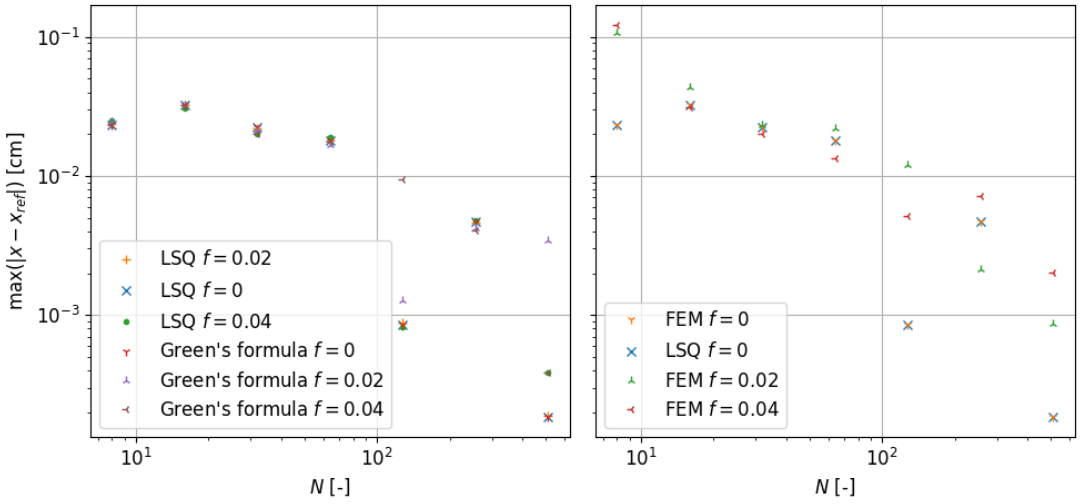

FIGURE 6.10: Maximum of the difference between the last intersection x coordinate and and the depth of interpenetration computed analytically median$|x - x_{\text{ref}}|$ over the 50 rays as a function of mesh configuration determined by N and f.

Analogously to the median, the maximum value of the error is compared in Figure 6.10. There is no clear dependence on the method nor the randomization factor. This supports the hypothesis that the maximum of the error mostly characterizes the effects of the finite dimensions of the cells. What is more problematic, is the fact, that there is not even a very clear decrease in the maximum of the error with decreasing cell size. It is concluded that the mesh imprinting effect is dominant in the area around $n_{\text{e}}^{\text{eff}}$, where the refraction angles are highest.

Considering the results, and also taking into account the ease of implementation, the least-squares method is the best candidate for the usage in the ray-tracing simulations. It is thus used throughout the rest of the work.

Chapter 7

Comparison with existing methods

In this chapter, a comparison of the previously used approaches and the current model is presented. First, a method known as the WKB approximation [28], used in code PETE2 [12], is analyzed and a special setup in which both methods are equal is described. Next, a full simulation is compared to the previous work [9] using the same simulation parameters.

7.1 Comparison with the WKB approximation

Previously, in the finite element code PETE2 [12], the WKB approximation [28] was used to model laser absorption. This approximation assumes the laser is propagating without focusation and practically an operator splitting technique is used to evaluate the source term in equation (2.6).

To compare it with the ray-tracing algorithm consider a 2D rectangular mesh 1 cell wide and an arbitrary number of cells long. Then, tracing a ray through the middle of this mesh along the axis results in the same source terms $\nabla \cdot \mathbf{S}$ as using the WKB approximation. In this case, ray-tracing can be thought of as a generalization to an arbitrary direction of propagation and enables the simulation of diffraction and refraction effects. On the other hand, this holds only for the lowest order finite elements. While the WKB approximation can be directly generalized to higher order elements, this is not the case for ray-tracing. The algorithm can be improved to the first order of interpolation with a linear profile of thermodynamic quantities in cells (usually called parabolic ray-tracing).

Otherwise, techniques involving projection on a finer mesh discussed in chapter 2 are necessary to achieve a higher order of precision.

7.2 Comparison with a finite difference simulation

In [9], the ray-tracing is used to simulate a laser target interaction in a finite difference hydrodynamic code [29]. We design a similar simulation using the finite element code and compare the results.

A single p-polarized laser pulse with wavelength 1315 nm impinges an aluminium target. The temporal profile of the pulse is a Gaussian with the time of arrival of maxima $\tau = 400\,\mathrm{ns}$ and width $\Delta^{\mathrm{t}}_{\mathrm{FWHM}} = 400\,\mathrm{ns}$ and maximum intensity $I_{\max} = 2.4 \times 10^{15}\,\mathrm{W \cdot cm^{-2}}$. The results are compared at time $t = 600\,\mathrm{ns}$. In the original work, a cylindricaly symmetrical geometry is used. In this geometry, the spatial profile of the pulse is a symmetrical 2D Gaussian with a focus radius $r_{\mathrm{f}} = 100\,\mu\mathrm{m}$. The focus radius can be identified with the parameter σ of the spatial Gaussian (4.5) and is related to the spatial FWHM $\Delta^{\mathrm{s}}_{\mathrm{FWHM}}$ in the following way

$$r_{\mathrm{f}} = \frac{\Delta^{\mathrm{s}}_{\mathrm{FWHM}}}{2\sqrt{2(\ln 2)}}. \tag{7.1}$$

As the cylindrical geometry is not supported in our simulation, we use a ratio between the maximal intensities derived in [30] to obtain a comparable result

$$\frac{I^{\mathrm{cyl}}_{\max}}{I^{\mathrm{cart}}_{\max}} \doteq 2.004 \tag{7.2}$$

The same ideal gas equation of state is used with the Poisson constant $\gamma = 5/3$. Furthermore, symmetry along y axis in Cartesian coordinates is assumed. Initially, the mesh is orthogonal with 50 cells in the x dimension and 25 cells in the y dimension. In both dimensions, a geometric coefficient leading to decreasing cell dimension is used. The smallest cell is on the target surface closest to the axis of symmetry.

Profiles of temperature T, mass density ρ, source term $\boldsymbol{\nabla \cdot S}$ (representing absorption) and velocity in the x dimension v_x are show in Figure 7.1 and for easier comparison the values of $\boldsymbol{\nabla \cdot S}$ are zoomed in Figure 7.2.

First, it must be noted that the value of $\boldsymbol{\nabla \cdot S}$ is dependant on the numerical time step and thus the absolute values are irrelevant for any evaluation, but the spatial profile can be studied. The maximal temperature in [9] is around 3000 eV, here it is closer to 5000 eV. In addition, the temperature profile in our simulation is significantly more

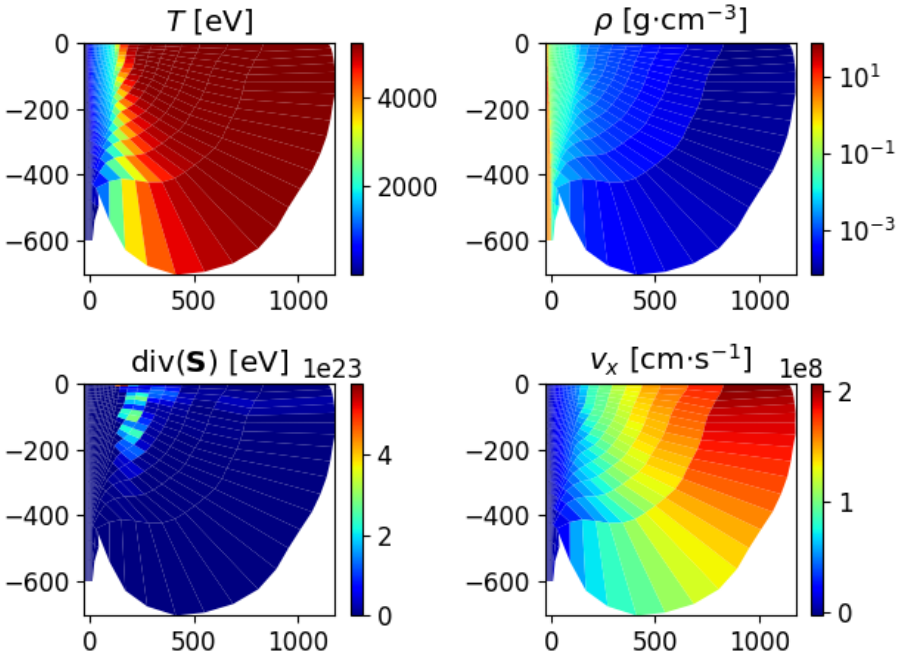

FIGURE 7.1: The resulting numerical values of temperature T, density ρ, absorption $\nabla \cdot \mathbf{S}$ and velocity in x dimension v_x at time $t = 600\,\text{ns}$ in a simulation of a laser interacting with an aluminium target with initial parameters taken from [9]

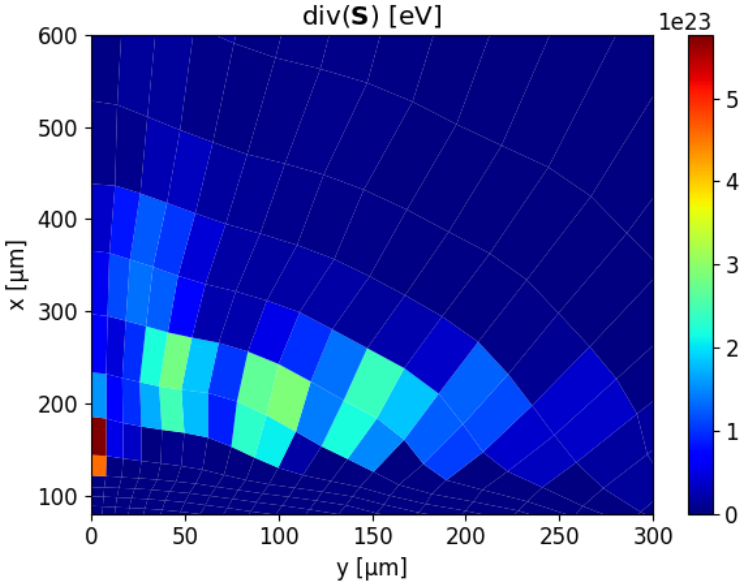

FIGURE 7.2: A zoom the absorbed energy $\nabla \cdot \mathbf{S}$ at time $t = 600\,\text{ns}$ in the simulation with initial parameters taken from [9]

diffused than in the referenced work, where a clear local maximum exists. The density scales are similar. Velocity can not be directly compared as it is not documented in [9], but it seems that the rate of expansion of our simulation is higher.

It is clear that the dynamics of the simulation is similar, but not the same as in [9]. The mesh successfully expands with the plasma corona and no significant oscillations in both, the node positions and thermodynamic variables are present. The differences can be partially attributed to the different geometries used in the simulations. Furthermore, there may be differences in calibration of models of the artificial viscosity, the heat transfer and the collision frequency calculation. All these models can influence the position at which the laser is absorbed and consequently influence the whole dynamics of the simulation.

Chapter 8

Simulation of realistic plasma with positive x-ray gain coefficient

In this chapter, a simulation of a particular driving laser configuration proposed in [10] is performed.

Here, more advanced model is used in the gain simulations. It employs the M level model for the gain calculation instead of the 3 level model used in [10]. A direct comparison of the models was shown in our previous work [6]. The main conclusion is that the predicted values of the gain coefficient are significantly lower in the M level model . The discrepancy originates directly from the solution of the rate equations and was previously addressed in [6].

Furthermore, several different models are used during the hydrodynamic simulation. The code described in this work employs the two-temperature approximation of the plasma instead of a single temperature model in [10]. The main difference is the use of the ray-tracing instead of the simpler model employed in [10], where the laser is assumed to be propagating along a straight line perpendicular to the surface of the target and accounted for in the energy equation (2.6) as a directly evaluated source term based on the laser intensity. The main advantage of hydrodynamic code used in [10] is given by an adaptive mesh refinement technique used there, that improves the accuracy of the solution during the simulation. Our simulation suffers from undesired effects originating from mesh entangling that could be mitigated using a similar technique. In both simulations, a quotidian equation of state (QEOS) [31] is used.

First pulse	Second pulse	Third pulse
$\tau = 1.5$ ns	$\tau = 2.0$ ns	$\tau = 2.51$ ns
$\Delta^{\mathrm{t}}_{\mathrm{FWHM}} = 1.0$ ns	$\Delta^{\mathrm{t}}_{\mathrm{FWHM}} = 0.1$ ns	$\Delta^{\mathrm{t}}_{\mathrm{FWHM}} = 0.5$ ps
$I_{\mathrm{max}} = 1.25 \cdot 10^{11}$ W·cm^{-2}	$I_{\mathrm{max}} = 1.25 \cdot 10^{12}$ W·cm^{-2}	$I_{\mathrm{max}} = 1.16 \cdot 10^{15}$ W·cm^{-2}

TABLE 8.1: Parameters of the incoming laser pulses, τ is the time of arrival, $\Delta^{\mathrm{t}}_{\mathrm{FWHM}}$ is full width at half maxima, and I_{max} is the maximum of intensity [6], [10]

8.1 Parameters of the simulation

The simulation involves three laser pulses of the driving laser. All the pulses have the same wavelength 800 nm and spatial profile. The spatial profile of the laser is the super-Gaussian (4.5) with $P = 10$ and varying $\Delta^{\mathrm{s}}_{\mathrm{FWHM}}$ across different simulations. Each pulse has a Gaussian temporal profile characterized by the peak intensity I_{max}, time of maxima arrival τ, and $\Delta^{\mathrm{t}}_{\mathrm{FWHM}}$. The temporal profiles of the pulses differ greatly and are summarized in table 8.1.

These three pulses have the following purpose: the first long laser pulse forms the plasma medium, ensuring a good absorption of the second shorter more intense pulse, which heats the plasma. The last pulse is almost instantaneous, compared to the previous two pulses and is also the most intense. The goal is to quickly heat up electrons and establish optimal conditions for the population inversion. The simulation is terminated 0.01 ns after the time of arrival of maximum of the last pulse and a snapshot of the hydrodynamic variables is taken.

The simulation is performed in the Cartesian 2D geometry on an initially orthogonal mesh with 55 cells in the x dimension and 60 cells in y dimension while assuming axial symmetry over the x-axis. The initial size of the cells in x-dimension is decreasing towards the target surface with the geometric factor q_{geom}. Surface of the target is located at $x = 0$ and the target is 10 µm iron slab. The target lies in the negative values of the x-axis. The dimensions of the target are set to provide a sufficient computational domain and do not necessarily reflect reality. The laser comes from positive x and initially interacts with the target at $x = 0$ (in figures it is propagated from right to left).

Simulations for the spatial profiles with $\Delta^{\mathrm{s}}_{\mathrm{FWHM}}$ equal to 200 µm, 150 µm, 100 µm and 75 µm were performed for the sake of comparison with [10]. The value of $\Delta^{\mathrm{s}}_{\mathrm{FWHM}}$ is further referred to simply as the width.

The geometric factor q_{geom} is the main optimization parameter when it comes to properly simulating the laser target interaction with sufficient resolution. With an excessively high factor the simulation crashes due to overlapping cells or too small time step estimated by (2.52). If the factor is too small, the whole laser is absorbed into a

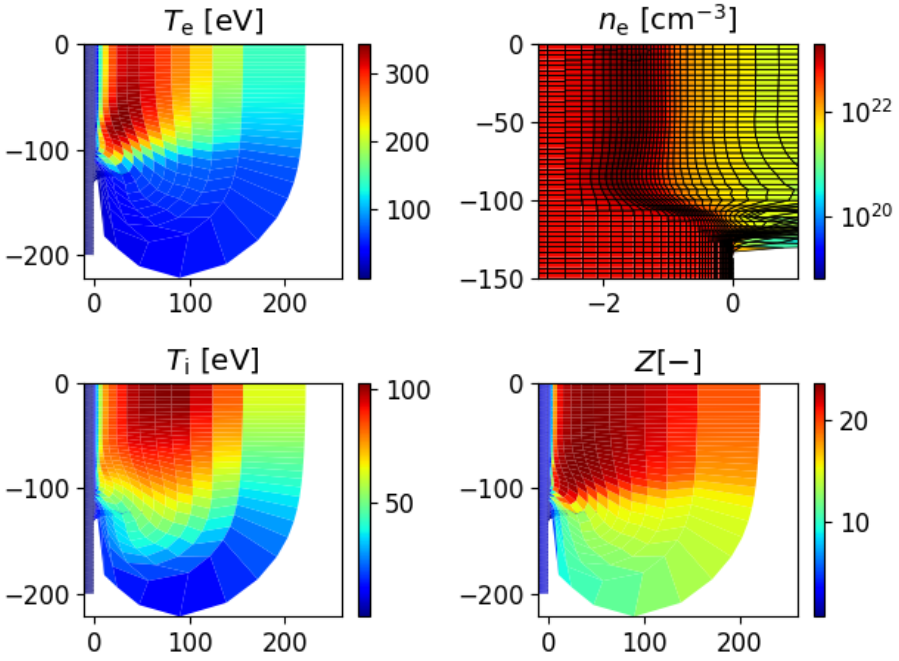

FIGURE 8.1: The numerical values of electron temperature T_e, ion temperature T_i, electron density n_e and mean ionization Z at time $t = 2.52\,\text{ns}$ in a simulation of the $200\,\mu\text{m}$ wide laser

few exceedingly expanding cells and the simulation resolution is too low to draw any useful conclusions. Different values were used for different simulations.

8.2 Results of the simulation

The values of electron temperature T_e, ion temperature T_i, electron density n_e and mean ionization Z at time $t = 2.52\,\text{ns}$ from a simulation of $200\,\mu\text{m}$ wide driving laser are in Figure 8.1. It must be stressed, that axial symmetry of the simulation is assumed. Comparing the results of the simulation with [10], it can be observed that we obtained lower temperature overall. The maximum of T_e is 342 eV, while in the one temperature model of [10] it is around 530 eV. The T_i maximum is approximately 103 eV. A clear difference between ion and electron temperatures is expected and results from the absorption of the last laser pulse. The laser pulses heat op electrons and the electrons, in turn, heat up ions through heat exchange as clearly seen from (2.6), (2.7). During and shortly after the last pulse electron-ion heat exchange is not fast enough to heat up the ions, as the pulse is shorter than a typical relaxation time. The maximum of the mean ionization Z is around 23.5. Electron density is highest in the target where a shock wave forms and is around $1.9 \times 10^{23}\,\text{cm}^{-3}$. In [10] the reported n_e is two orders of magnitude lower, even though the profile is similar. Our value seems to be reasonable for this kind of

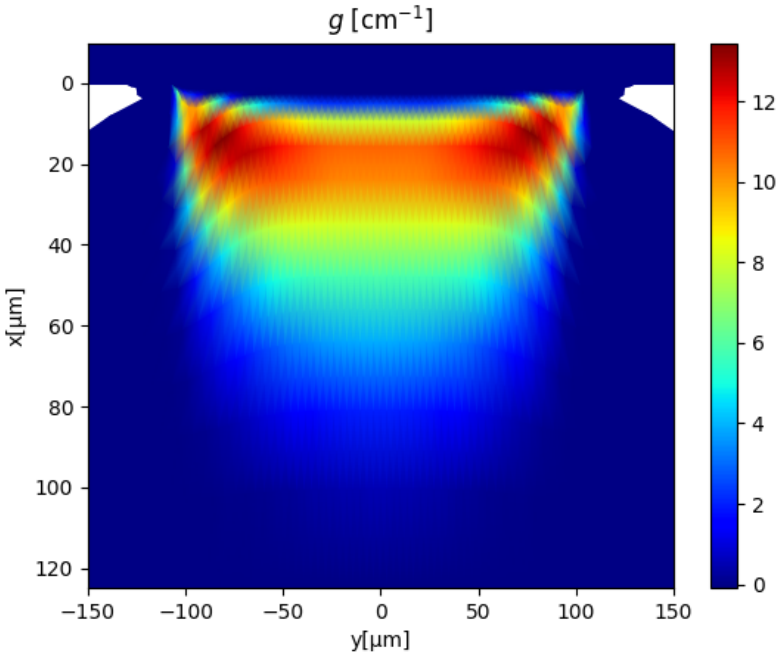

FIGURE 8.2: Gain coefficient g at time $t = 2.52\,\text{ns}$ obtained by post-processing a simulation of 200 µm wide laser interacting with a solid Fe target

simulation, based on results from other codes [7], [9] and the source of this discrepancy is not clear.

The four thermodynamic variables summarized in the figure are then used as an input for the M-level model of the gain coefficient described in chapter 5. A 2D profile of gain coefficient is obtained. Furthermore, the whole plasma corona is reconstructed using the axial symmetry for further evaluation. The result is shown in Figure 8.2. The image is rotated in such a way that the target is on top and the laser comes from the bottom side, to enable direct comparison with [10].

As already mentioned, the gain coefficient g predicted by the M level model is much lower then in [10]. The maximum values is $13.4\,\text{cm}^{-1}$ for the laser 200 µm wide laser. Apart from the absolute value, the shape of the gain profile is remarkably similar.

Results of the simulations for laser widths 150 µm, 100 µm and 75 µm are processed analogously. Only the mean ionization is omitted as its profile is not of particular interest and the gain g is included in the summary of thermodynamic variables instead. The results for 150 µm, 100 µm laser width are almost identical to the results obtained for 200 µm wide laser, apart from a scale factor. The result for 100 µm laser is taken to illustrate both configurations in Figure 8.3.

Simulation with laser width 75 µm leads to an excessively deformed mesh. This effect occurs at the edge of the super-Gaussian pulse. A very similar effect for purely

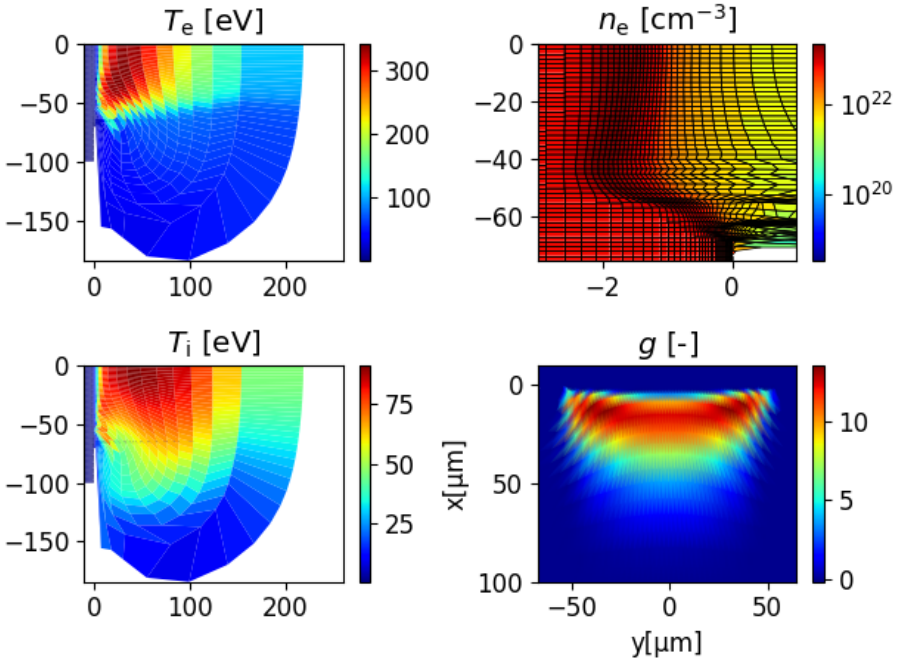

FIGURE 8.3: Values of electron temperature T_e, ion temperature T_i, electron density n_e and gain coefficient g at time $t = 2.52$ ns in a simulation of 100 µm wide laser interacting with a solid Fe target

Δ^s_{FWHM} [µm]	75	100	150	200
g_{max} [cm^{-1}]	14.3	13.56	13.57	13.44

TABLE 8.2: Maximum gain values for various driving laser widths Δ^s_{FWHM}

Lagrangian simulations was observed in [30] for disc flyer impact simulations. As pointed out in [10], 2D effects are more relevant for narrower lasers. These effects probably lead to the shear motion of the mesh and result in the mesh deformation. Same effect, can be seen (to a much lesser extent) in the other simulations. Implementation of an ALE scheme [30] would probably resolve the issue. The resulting variables are shown in Figure 8.4. In the profile of T_i a non-physical extreme is starting to form and the mesh is severely overlapped. The overlapping of the mesh can be seen in Figure 8.5.

The maximum gain coefficient g_{max} for all 4 simulations is summarized in table 8.2 for each of the laser widths. The value for laser width 75 µm is probably not physical and results from the simulation failure.

To summarize, the simulations of wider lasers are in agreement with the results in [10], apart from the absolute value of gain coefficient g. It is also concluded that implementation of an adaptive mesh refinement technique or ALE is desirable to harness the full potential of the code.

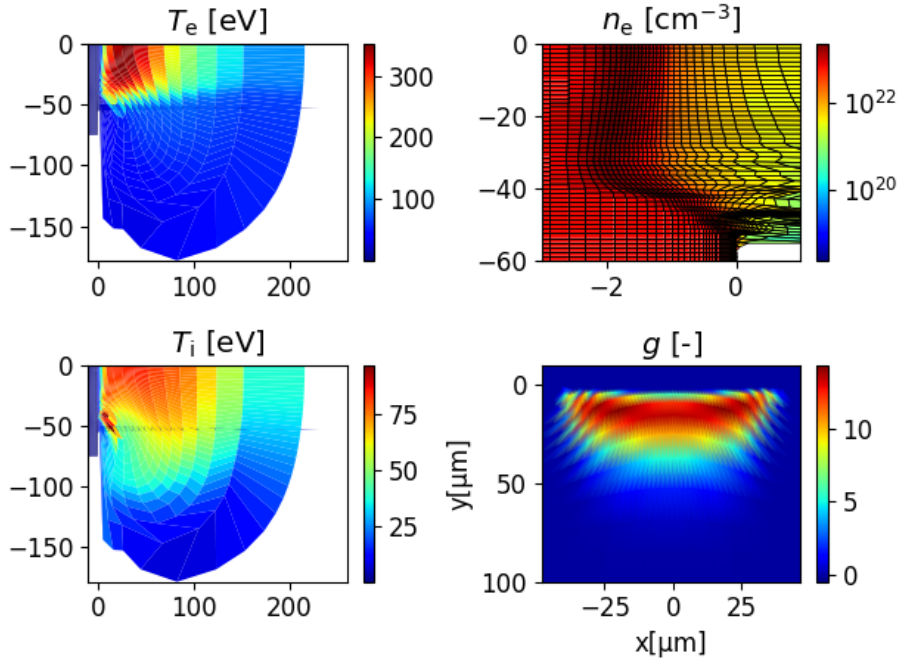

FIGURE 8.4: Values of electron temperature T_e, ion temperature T_i, electron density n_e and gain coefficient g at time $t = 2.52$ ns in a simulation of 75 µm wide laser interacting with a solid Fe target

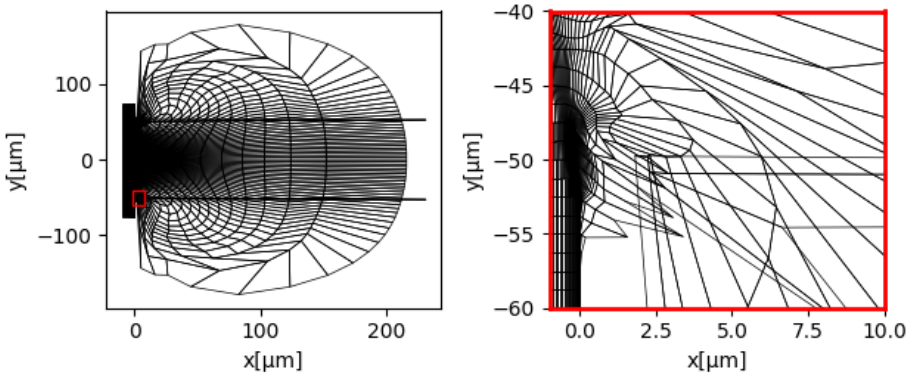

FIGURE 8.5: Mesh overlapping and invalid zone formation in a simulation of 75 µm wide laser interacting with a solid Fe target

Chapter 9

Evaluation of the diffraction effects in x-ray propagation

The diffraction of the seeding laser pulse is studied based on the results of the simulations with configurations described in the previous chapter 8. Several problems are identified, which arise during the simulation and represent a significant difficulty. Multiple possible solutions to these problems are proposed, their feasibility is discussed and finally, a semi-analytic approach is used to study the diffraction effects influencing the x-ray seeding pulse. The results are then compared with the previous studies [32], [33].

9.1 Difficulties using the linear ray-tracing algorithm to estimate diffraction

The results of simulations for various widths of the driving laser were presented in the previous chapter 8. The regions on the edge of the laser beam are studied in terms of diffraction of the seeding pulse. For that, an instantaneous traversal of a seeding pulse with wavelength of 25.5 nm is assumed and the trajectory of the pulse is studied. We have chosen the pulse, to fully cover gain zone of the plasma. It has a Gaussian profile with spatial $\Delta^{\mathrm{s}}_{\mathrm{FWHM}} = 50\,\mu\mathrm{m}$ in the direction almost parallel to the target surface. An angle between the target surface and the laser direction is 5 mrad towards the target. The pulse is divided into 1000 individual rays. The initial power of the laser is set to $1\,\mathrm{J}\cdot\mathrm{s}^{-1}$ (a value designed to simplify the interpretation of results).

The ray trajectories and the power used for the x-ray amplification are shown in Figure 9.1. Not all trajectories are depicted, instead, the first and then each 40th trajectory is plotted. It turns out that no diffraction is happening at the edge of the

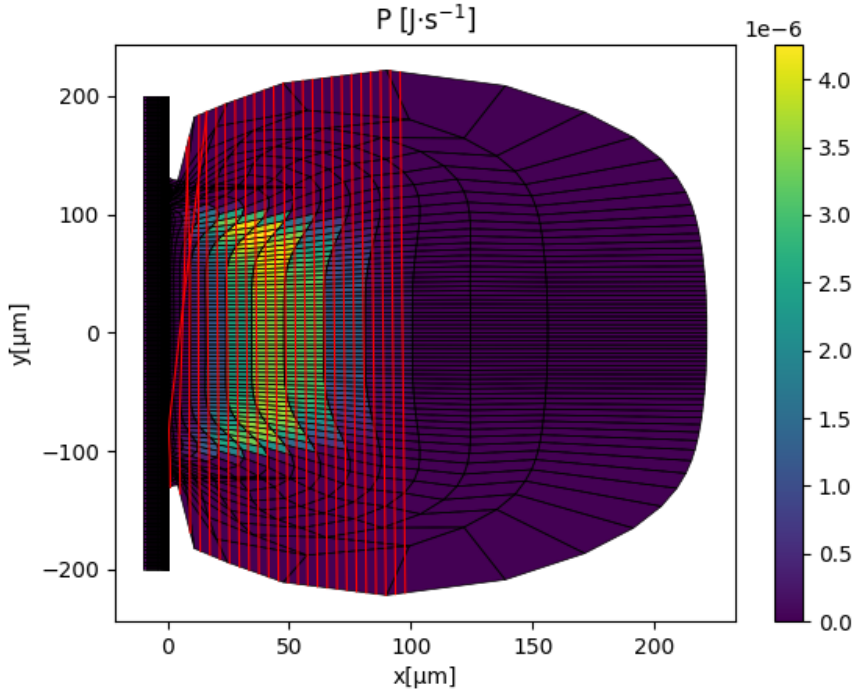

FIGURE 9.1: Rays of the seeding pulse propagating parallel to the target surface in a plasma produced by 200 µm wide laser. The first and then each 40th ray is shown.

denser zone of the plasma corona. The only diffraction effects are observed near the initial target surface. This is not of a particular interest, as the rays near the target surface are not passing through the gain zone and are not significantly amplified. It may lead to marginal focusing of the radiated power, but we are more interested in diffraction inside the gain zone.

To actually study diffraction in the gain zone, we would need a much wider plasma. This is easy to obtain because we have shown that the dynamics of the simulation do not change when increasing the plasma width. We may just repeat the cells closest to the axis to artificially widen the plasma. This is a reasonable approximation because the plasma is homogeneous in the y direction near the axis of symmetry.

Unfortunately, the resulting mesh is not fine enough to be able to study the diffraction effects in detail. The gain zone spans over only a few cells. Any set of rays almost parallel to the target surface traced using a linear ray-tracing algorithm would simply pass through the mesh without ever encountering a face parallel with the target. This would lead to little or no diffraction even though the rays should continuously diffract while traversing the cells in reality. We were not able to obtain any more detailed simulation using the code PETE2 [12] as the initial mesh has already a very low value of the geometric factor. Any smaller value resulted in too small time steps or the simulation crashing immediately due to extreme volume ratios.

Several options are available to address the issue. First is a formulation of the hydrodynamics using the arbitrary Lagrangian-Eulerian method (ALE) or employing an adaptive mesh refinement technique to resolve the issues with the hydrodynamic simulations. Another option is to use a parabolic ray-tracing algorithm or directly integrating the ray trajectory inside the cell. None of the mentioned approaches are implemented in the PETE2 code [12] and are beyond the scope of this work.

9.2 Semi-analytic approach to the estimation of the diffraction effects

We propose a semi-analytic approach to at least partially overcome the issues identified in the previous section. Is has been already recognized that the plasma is homogeneous in the y direction near the axis of symmetry. This means that the plasma can be described using profiles of thermodynamic quantities dependent on x only. The discrete electron density profile $n_\mathrm{e}(x)$ is taken and a linear interpolation is employed. A piece-wise constant gradient of this profile is then calculated. The gradient in a cell is calculated from the value of n_e in the cell and a cell next to it on the left (lower x coordinate value). This is performed for each of the cells, except the last one with lowest value of x coordinate. Such assignment is clearly not optimal, but is reasonable enough for our approximation.

The analytic solution (3.25) of the eikonal equation is used to obtain the trajectory of a single ray with wavelength 25.5 nm in each part of the profile with the constant gradient. The trajectories are shown in Figure 9.2 in a piece-wise constant density profile homogeneous in y (original electron density profile, before the employment of the linear approximation). The y value where the ray leaves the zone is in this work called the diffraction scale because it represents the distance at which we may expect the diffraction to be significant enough for the ray to leave the zone of constant gradient.

In the Figure 9.3, the diffraction scale profile is compared with the gain profile. It is clear that even for the zone closest to the target, where the gain is very small around $2\,\mathrm{cm}^{-1}$, it is not reasonable to expect diffraction effect to play a major role for the plasma width of less than roughly 400 µm. In reality, it is more reasonable to expect that diffraction effects will appear for the plasma of widths around 1800 µm, where the diffraction would start to influence the rays passing through the zone of maximal gain. Probably, at least twice as wide plasma may be the limit where the amplification of the seeding pulse may be affected by diffraction, simply because a portion of the pulse will always be refracted into the zone of the maximal gain.

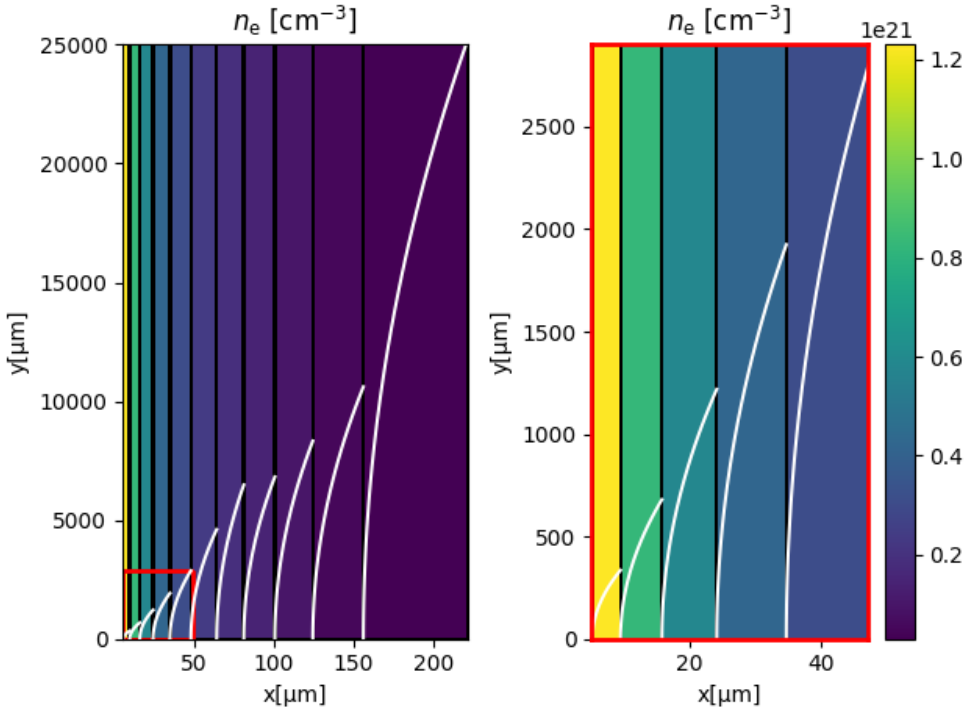

FIGURE 9.2: Analytic solutions of the eikonal equation in zones with constant electron density gradient profile for rays initially parallel to the target surface with values of electron density n_e in the background

In [33], a similar situation is studied with analogous gradient and gain profiles. There it is concluded, that the diffraction starts to limit the x-ray amplification for plasma width around 4000 µm using a more sophisticated approach based on numerical integration techniques. This corresponds well with our approximate orders of magnitude estimation.

Finally, divergence of the resulting rays can be an estimated. It is assumed that some amplified rays are not refracted too much after passing through the plasma in the part of the gain zone, where the diffraction effects are low (right side). On the other hand the most curved rays will result from the rays closest to the target that are still passing through a zone of positive gain. Using an approximation, $\tan(\theta) \approx \theta$ for $\theta << 1$ for the angle of the rays closest to the target and assuming the ray is a straight line an angle between the rays leaving the plasma and the target surface can be estimated. These assumptions are valid because the diffraction scale is much larger than the zone dimension. The biggest angle is obtained for the zone with positive g closest to the target. The zone is 6.3 µm wide and the diffraction scale is 680 µm for a ray originating at position $x = 9.4$ µm. The divergence angle is ~ 9 mrad. This is close to the value ~ 8 mrad estimated by [32] in a similar configuration.

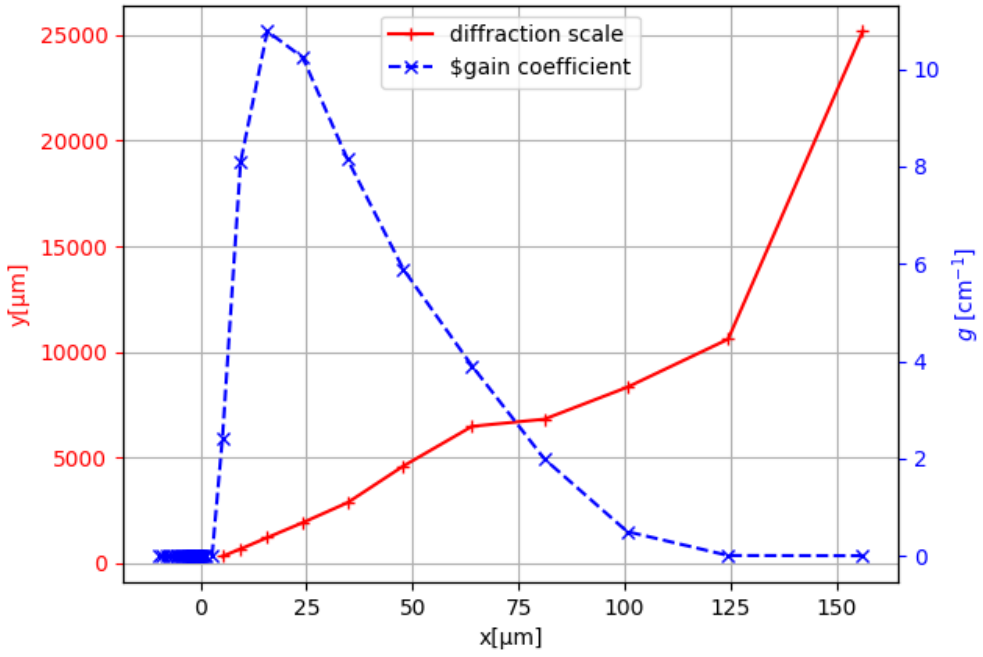

FIGURE 9.3: Diffraction scale and gain coefficient profile g as a function of the distance x from the initial target surface $x = 0$

Chapter 10

Conclusion

The aim of this thesis is to investigate the plasma produced by a laser beam interacting with a solid target as a possible candidate for the gain medium of an x-ray laser. The main goal of the study is to develop the necessary tools to enable sophisticated simulations of plasma formation and soft x-ray radiation amplification in the medium. The hydrodynamic description of the plasma dynamics based on the finite element formulation is extended by a ray-tracing algorithm, equipped with several models of power exchange and ability to evaluate the diffraction effects influencing the x-ray pulse amplification.

First, the theory concerning the formulation of Euler equations in the finite element method framework is reviewed. The models used to simulate heat transfer and collision frequency are summarized. Next, a model of artificial viscosity and a time stepping scheme are presented.

A whole chapter is dedicated to the ray-tracing algorithm for a laser propagating in the plasma described by a hydrodynamic simulation. There, not only the implementation of the method, but also the construction of analytic and numeric tests from the fundamental equations of the geometrical optic are described. The importance of electron density gradient calculation is emphasized as it governs the inner workings of the procedure.

Models of absorption via inverse bremsstrahlung and resonance are reviewed, continuing the description of the laser-plasma interaction. Furthermore, a model based on Fresnel equations is proposed to more precisely capture the physical phenomena occurring during the initial stages of the simulation.

The x-ray radiation amplification model developed in previous works is reviewed [6]. Through this model, the lasing properties are connected with thermodynamic quantities computed by the hydrodynamic simulation. It is based on a calculation of the populations of M possible energy levels in the plasma atoms, and used to post-process the results of the hydrodynamic simulations and determine the gain coefficients in the plasma.

Next, the developed ray-tracing algorithm together with several gradient calculation methods is tested on a simple problem with a linear profile of index of refraction. The convergence and robustness of the method are verified by the employment of several different mesh configurations including both regular and irregular grids with varying numbers of segments. The ray trajectory directly influences where and how is the laser power absorbed and is identified as a key factor of possible differences in absorption profiles. In turn, the gradient calculation directly impacts the trajectory finding procedure. The least-squares formulation of the gradient calculation is identified as the best of the three methods presented. Both, in terms of convergence and ease of implementation.

A comparison between the WKB approximation used in the simulations of laser propagation [12] and the developed ray-tracing algorithm is made. The advantages and disadvantages of both approaches are discussed. To fully test the whole code including all the implemented models and to compare it with previous results obtained using a finite difference scheme [29], a simulation of a laser impacting an aluminum target is performed. The results are compared and possible sources of discrepancies are discussed.

To fully utilize the potential of the implemented models, a hydrodynamic simulation concerning the preparation of plasma conditions with a positive gain coefficient for x-ray pulse amplification is performed. A solid Fe target interacting with an intense laser is studied in a 2D Cartesian hydrodynamic simulation with ray-tracing used to model the laser plasma interaction. The results are post-processed using the M-level model of gain coefficient estimation and compared with literature [10].

Finally, the seeding x-ray pulse propagation and amplification are addressed. Because only weak diffraction effects are identified in the simulation of a 200 µm wide laser, several conclusions are drawn about the study of diffraction effects of x-ray laser propagating in plasma. These conclusions lead to the creation of a semi-analytical model describing the diffraction, based on the results of previous simulations. The results obtained by this model are used to predict the width of the target necessary for the diffraction effects to play a major role in x-ray amplification. This is in good agreement with [33]. Further comparison is made with [32] using the estimation of the beam divergence, which is also in good agreement.

This work is the first step towards combining FEM hydrodynamic simulations with a ray-tracing algorithm. An implementation of a method of projection onto finer meshes, enabling the ray-tracing algorithm to work with high-order finite element hydrodynamic simulations is a possible topic of future research, to harness the full potential of the approach. Also, a parabolic ray-tracing procedure is expected to improve the laser diffraction calculation and can fully enable detailed x-ray laser amplification simulations. Finally, extending the FEM hydrodynamic simulations by employing an the Arbitrary-Lagrangian-Eulerian approach or using the techniques of adaptive mesh refinement, can improve rubustness of the simulations.

Bibliography

1. JAEGLE, Pierre. *Coherent Sources of XUV Radiation*. New York, NY: Springer New York, 2006. Optical Sciences. ISBN 9780387230078.
2. MORLENS, Anne-Sophie; GAUTIER, Julien; REY, Gilles; ZEITOUN, Philippe; CAUMES, Jean-Pascal; KOS-ROSSET, Marylène; MERDJI, Hamed; KAZAMIAS, Sophie; CASSOU, Kevin; FAJARDO, Marta. Submicrometer digital in-line holographic microscopy at 32 nm with high-order harmonics. *Optics Letters*. 2006, vol. 31, no. 21, pp. 3095–3097. ISSN 1539-4794.
3. HUANG, Zhirong; KIM, Kwang-Je. Review of x-ray free-electron laser theory. *Physical Review Special Topics - Accelerators and Beams*. 2007, vol. 10, no. 3, p. 034801.
4. RUS, B.; MOCEK, T.; PRÄG, A. R.; KOZLOVÁ, M.; JAMELOT, G.; CARILLON, A.; ROS, D.; JOYEUX, D.; PHALIPPOU, D. Multimillijoule, highly coherent x-ray laser at 21 nm operating in deep saturation through double-pass amplification. *Physical Review A*. 2002, vol. 66, no. 6, p. 063806.
5. ZEITOUN, Ph; FAIVRE, G.; SEBBAN, S.; MOCEK, T.; HALLOU, A.; FAJARDO, M.; AUBERT, D.; BALCOU, Ph; BURGY, F.; DOUILLET, D.; KAZAMIAS, S.; LACHÈZE-MUREL, G. de; LEFROU, T.; PAPE, S. le; MERCÈRE, P.; MERDJI, H.; MORLENS, A. S.; ROUSSEAU, J. P.; VALENTIN, C. A high-intensity highly coherent soft X-ray femtosecond laser seeded by a high harmonic beam. *Nature*. 2004, vol. 431, no. 7007, pp. 426–429. ISSN 1476-4687.
6. ŠACH, M. *Multidimensional Hydrodynamic Plasma Simulations and X-Ray Radiation Generation*. 2020. Research report. Czech Technical University in Prague.
7. ŠACH, M. *Hydrodynamic Plasma Simulations for X-Ray Laser Realization*. 2019. Bachelor's thesis. Czech Technical University in Prague.
8. KAISER, Thomas B. Laser ray tracing and power deposition on an unstructured three-dimensional grid. *Physical Review E*. 2000, vol. 61, no. 1, pp. 895–905.
9. VELECHOVSKÝ, J. *Modelling of Laser Radiation Absorption in Plasma*. 2010. Research report. Czech Technical University in Prague.

10. OLIVA, E.; ZEITOUN, P.; VELARDE, P.; FAJARDO, M.; CASSOU, K.; ROS, D.; SEBBAN, S.; PORTILLO, D.; PAPE, S. le. Hydrodynamic study of plasma amplifiers for soft-x-ray lasers: A transition in hydrodynamic behavior for plasma columns with widths ranging from 20μm to 2 mm. *Physical Review E*. 2010, vol. 82, no. 5, p. 056408.

11. DOBREV, Veselin A.; KOLEV, Tzanio V.; RIEBEN, Robert N. High-order curvilinear finite element methods for Lagrangian hydrodynamics. *SIAM Journal on Scientific Computing*. 2012, vol. 34, no. 5, B606–B641. ISSN 1064-8275, ISSN 1095-7197.

12. NIKL, J.; KUCHAŘÍK, M.; HOLEC, M.; WEBER, S. Curvilinear high-order Lagrangian hydrodynamic code for the laser-target interaction. In: CODA, S.; BERNDT, J.; LAPENTA, G.; MANTSINEN, M.; MICHAUT, C.; WEBER, S. (eds.). *Europhysics Conference Abstracts – 45th EPS Conference on Plasma Physics*. European Physical Society, 2018, vol. 42A, P1.2019. ISBN 979-10-96389-08-7.

13. ANDERSON, R.; ANDREJ, J.; BARKER, A.; BRAMWELL, J.; CAMIER, J. S.; CERVENY, J.; DOBREV, V.; DUDOUIT, Y.; FISHER, A.; KOLEV, T.; PAZNER, W.; STOWELL, M.; TOMOV, V.; AKKERMAN, I.; DAHM, J.; MEDINA, D.; ZAMPINI, S. MFEM: A modular finite element methods library. *Computers & Mathematics with Applications*. 2020. ISSN 08981221.

14. NIKL, J. *Some Aspects of Numerical Methods for Laser Plasma Hydrodynamics*. 2017. Master's thesis. Czech Technical University in Prague.

15. SPITZER, Lyman; HÄRM, Richard. Transport phenomena in a completely ionized gas. *Physical Review*. 1953, vol. 89, no. 5, pp. 977–981.

16. EIDMANN, K.; MEYER-TER-VEHN, J.; SCHLEGEL, T.; HÜLLER, S. Hydrodynamic simulation of subpicosecond laser interaction with solid-density matter. *Physical Review E*. 2000, vol. 62, no. 1, pp. 1202–1214.

17. BORN, Max; WOLF, Emil. *Principles of Optics: Electromagnetic Theory of Propagation, Interference and Diffraction of Light*. 6th ed. Oxford ; New York: Pergamon Press, 1980.

18. MALÝ, Petr. *Optika*. Prague: Karolinum, 2008. ISBN 9788024627939. OCLC: 1225203413.

19. GLASSNER, Andrew S.; ASSOCIATION FOR COMPUTING MACHINERY (eds.). *An introduction to ray tracing*. Digital print. San Francisco, Calif: Kaufmann, 2007. ISBN 9780122861604.

20. PERT, G. J. The analytic theory of linear resonant absorption. *Plasma Physics*. 1978, vol. 20, no. 3, pp. 175–188. ISSN 0032-1028.

21. HOLDEN, P. B.; HEALY, S. B.; LIGHTBODY, M. T. M.; PERT, G. J.; PLOWES, J. A.; KINGSTON, A. E.; ROBERTSON, E.; LEWIS, C. L. S.; NEELY, D. A computational investigation of the neon-like germanium collisionally pumped laser. *Journal of Physics B: Atomic, Molecular and Optical Physics*. 1994, vol. 27, no. 2, pp. 341–367. ISSN 0953-4075, ISSN 1361-6455.

22. GU, M. F. The flexible atomic code. *Canadian Journal of Physics*. 2008, vol. 86, no. 5, pp. 675–689. ISSN 0008-4204.

23. ABDELAZIZ, W. S. Calculation of atomic data and gain coefficient for XUV & soft x-ray laser emission from Ge XXIII. *Optics and Photonics Journal*. 2014, vol. 04, no. 09, pp. 246–269. ISSN 2160-8881, ISSN 2160-889X.

24. SHASHKOV, Mikhail. *Conservative Finite-Difference Methods on General Grids*. 2nd ed. Ed. by STEINBERG, Stanly. CRC Press, 2018. ISBN 9781315140209.

25. NISHIKAWA, H.; WHITE, J. A. An efficient cell-centered finite-volume method with face-averaged nodal-gradients for triangular grids. *Journal of Computational Physics*. 2020, vol. 411, p. 109423. ISSN 0021-9991.

26. KUCHAŘÍK, Milan; SHASHKOV, Mikhail. Conservative multi-material remap for staggered multi-material Arbitrary Lagrangian–Eulerian methods. *Journal of Computational Physics*. 2014, vol. 258, pp. 268–304. ISSN 0021-9991.

27. STEWART, G. W. *Matrix Algorithms*. Society for Industrial and Applied Mathematics, 1998. Other Titles in Applied Mathematics. ISBN 9780898714142.

28. RAMIS, R.; EIDMANN, K.; MEYER-TER-VEHN, J.; HÜLLER, S. MULTI-fs – A computer code for laser–plasma interaction in the femtosecond regime. *Computer Physics Communications*. 2012, vol. 183, no. 3, pp. 637–655. ISSN 0010-4655.

29. LISKA, R.; KUCHAŘÍK, M.; LIMPOUCH, J.; RENNER, O.; VÁCHAL, P.; BEDNÁRIK, L.; VELECHOVSKÝ, J. ALE method for simulations of laser-produced plasmas. In: FOŘT, Jaroslav; FÜRST, Jiří; HALAMA, Jan; HERBIN, Raphaèle; HUBERT, Florence (eds.). *FVCA VI*. Berlin, Heidelberg: Springer, 2011, vol. 2, pp. 57–73. Springer Proceedings in Mathematics. ISBN 9783642206719.

30. KUCHAŘÍK, M. *Arbitrary Lagrangian-Eulerian (ALE) Methods in Plasma Physics*. Prague, 2006. Phd thesis. Czech Technical University in Prague.

31. MORE, R. M.; WARREN, K. H.; YOUNG, D. A.; ZIMMERMAN, G. B. A new quotidian equation of state (QEOS) for hot dense matter. *The Physics of Fluids*. 1988, vol. 31, no. 10, pp. 3059–3078. ISSN 0031-9171.

32. PLOWES, J. A.; PERT, G. J.; HEALY, S. B.; TOFT, D. T. Beam modelling for x-ray lasers. *Optical and Quantum Electronics*. 1996, vol. 28, no. 3, pp. 219–228. ISSN 0306-8919, ISSN 1572-817X.

33. LE PAPE, S; ZEITOUN, Ph. Modeling of the influence of the driving laser wavelength on the beam quality of transiently pumped X-ray lasers. *Optics Communications*. 2003, vol. 219, no. 1, pp. 323–333. ISSN 0030-4018.